

Supporting Information

SHG-active NIR-emissive molecular nanomagnets generated in layered neodymium(III)-octacyanidometallate(IV) frameworks

Robert Jankowski,^a Jakub J. Zakrzewski,^a Mikołaj Zychowicz,^a Junhao Wang,^b Yurie Oki,^b
Shin-ichi Ohkoshi,^{*b} Szymon Chorazy^{*a} and Barbara Sieklucka^{*a}

^aFaculty of Chemistry, Jagiellonian University, Gronostajowa 2, 30-387 Krakow, Poland.

^bDepartment of Chemistry, School of Science, The University of Tokyo, 7-3-1 Hongo, Bunkyo-ku, Tokyo 113-0033, Japan.

Corresponding authors: chorazy@chemia.uj.edu.pl; ohkoshi@chem.s.u-tokyo.ac.jp; barbara.sieklucka@uj.edu.pl

Figure S1.	Infrared (IR) absorption spectra of 1 and 2 .	S2
Figure S2.	Thermogravimetric (TG) curves of 1 and 2 .	S3
Table S1.	Crystal data and structure refinement for two enantiomeric forms of 1 (1a and 1b).	S4
Figure S3.	The asymmetric units of 1a and 1b shown with the atoms labelling scheme.	S5
Figure S4.	Graphical presentation of the static structural disorder in 1 related to pzdo ligands.	S6
Table S2.	Results of CShM analysis for Mo ^{IV} and Nd ^{III} coordination spheres.	S7
Table S3.	Detailed structural parameters of Nd1 and Nd2 complexes in 1a and 1b .	S8
Figure S5.	Experimental P-XRD pattern of 1 compared with the simulated P-XRD pattern obtained from the LeBail fitting procedure performed using an EXPO 2014 software.	S10
Table S4.	Comparison of the unit cell parameters of 1a and 1b with the bulk samples of 1 and 2 .	S10
Table S5.	The comparison of structures and properties of the selected Ln ^{III} -[Mo ^{IV} /W ^{IV} (CN) ₈] ⁴⁻ systems.	S11
Figure S6.	Visualization of anion- π interactions in 1 .	S12
Figure S7.	The schematic presentation of the experimental setup used for SHG measurements.	S13
Figure S8.	Wavelength dependences of the SH signal for 1,2 , and the reference of KDP, together with the photos of the respective samples in the experimental setup and the detected SH light.	S14
Figure S9.	The SH intensity versus excitation power dependences for 1, 2 , and KDP.	S15
Figure S10.	Solid-state UV-vis absorption spectra of 1 and 2 .	S16
Table S6.	Results of the deconvolution carried out for the solid-state absorption spectra of 1 and 2 .	S16
Figure S11.	Direct-current (<i>dc</i>) magnetic characteristics of 1 and 2 .	S17
Figure S12.	Magnetic-field-variable alternate-current (<i>ac</i>) magnetic susceptibility characteristics of 1 .	S18
Figure S13.	Temperature-variable alternate-current (<i>ac</i>) magnetic susceptibility characteristics of 1 .	S19
Figure S14.	Magnetic-field-variable alternate-current (<i>ac</i>) magnetic susceptibility characteristics of 2 .	S20
Figure S15.	Temperature-variable alternate-current (<i>ac</i>) magnetic susceptibility characteristics of 2 .	S21
	Comment to Figures S12–S15.	S22
Figure S16.	The Arrhenius-type fitting of the limited part of the temperature-dependences of magnetic relaxation time for 1 and 2 .	S23
Figure S17.	Temperature dependences of magnetic relaxation time for 1 and 2 shown with the fitted contributions from Raman, direct, and QTM relaxation processes.	S24
Figure S18.	Visualization of the structural fragments of 1a used for the <i>ab initio</i> calculations.	S25
Table S7.	Description of the basis sets employed in the <i>ab initio</i> calculations for 1a .	S26
Table S8.	The energy splitting of the ground ⁴ I _{9/2} multiplet of Nd ^{III} centers in 1a .	S26
Table S9.	Pseudo- <i>g</i> -tensor components for all Kramers doublets of Nd ^{III} ground multiplets in 1a .	S27
Table S10.	Composition of the ground Kramers doublets of Nd ^{III} centres of 1a shown in the <i>m_j</i> basis.	S28
Table S11.	The crystal-field parameters of Nd1 complex in 1a obtained from the <i>ab initio</i> calculations.	S29
Table S12.	The crystal-field parameters of Nd2 complex in 1a obtained from the <i>ab initio</i> calculations.	S30
Table S13.	The crystal-field parameters of Nd2' complex in 1a obtained from the <i>ab initio</i> calculations.	S31
Figure S19.	Correlation of the results of the <i>ab initio</i> calculations with the emission spectrum of 1 .	S32

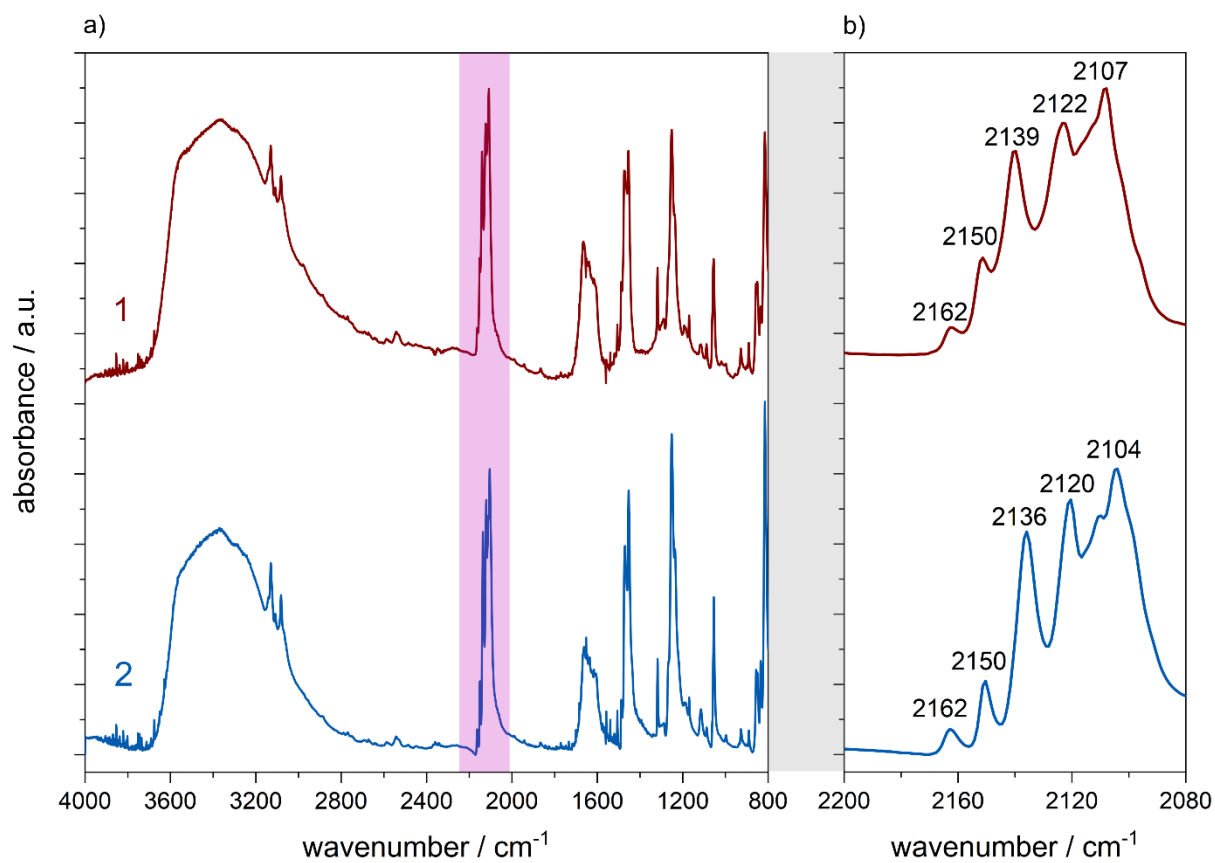


Fig. S1 Infrared (IR) absorption spectra of the selected single crystals of **1** and **2** collected in the 4000–800 cm^{-1} wavenumber range (a), presented together with the enlargement of the 2200–2080 cm^{-1} region assignable to the stretching vibrations of cyanido ligands (b).

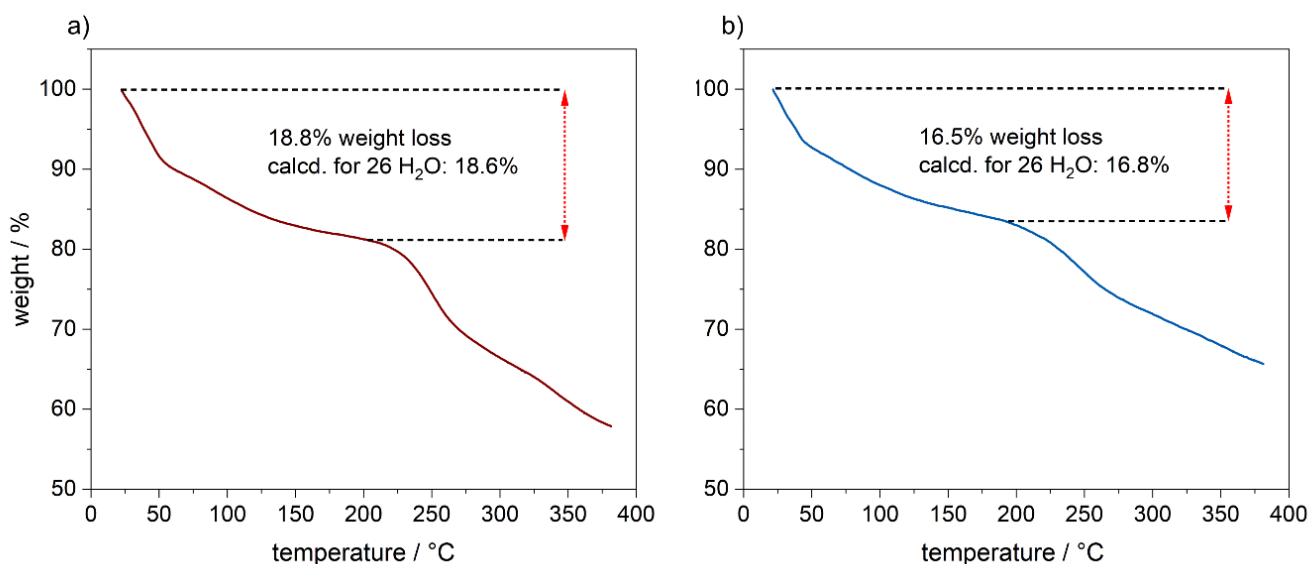


Fig. S2 Thermogravimetric (TG) curves of **1** (a) and **2** (b) gathered under nitrogen atmosphere in the 22–375 °C temperature range. The weight losses ascribable to the removal of water molecules were indicated on the graph.

Comment to Fig. S2:

The gradual decrease of the sample masses of **1** and **2**, occurring upon heating from room temperature up to ca. 200 °C can be ascribed to the removal of both water of crystallization as well as water coordinated to Nd^{III} centers. The related weight losses agree well with the expected total number of 26 water molecules per the {Nd^{III}₄M^{IV}₃} (M = Mo for **1**, M = W for **2**) formula unit. The initial sharp steps below 50 °C can be assigned to the release of weakly bonded water molecules of crystallization. Upon heating above 50 °C, the decrease in the samples' masses slows but it is continuously observed down up to ca. 200 °C. After exceeding this point, a rapid mass drop is observed which can be related to the removal of organic and/or cyanido ligands which presumably results in the decomposition of the samples. It is important to note that the courses of TG curves for **1** and **2** are very similar indicating almost identical thermal stability of the obtained coordination frameworks being only little dependent on the applied octacyanidometallate anions.

Table S1 Crystal data and structure refinement for two enantiomeric forms of **1** (**1a** and **1b**).

	1a	1b
CCDC no.	2061390	2061391
formula	C ₄₄ H ₇₂ Mo ₃ N ₃₄ Nd ₄ O ₃₆	
formula weight / g·mol⁻¹	2518.13	
temperature / K	100(2)	
crystal system	monoclinic	
space group	C2	
<i>a</i> / Å	47.022(2)	47.052(3)
<i>b</i> / Å	9.0142(4)	9.0064(5)
<i>c</i> / Å	9.7443(4)	9.7326(5)
β / °	100.4000(10)	100.309(2)
volume / Å³	4062.4(3)	4057.8(4)
Z	2	
ρ_{calc} / g·cm⁻³	2.059	
absorption coefficient / cm⁻¹	3.062	3.065
<i>F</i>(000)	2456	
crystal size / mm x mm x mm	0.2 x 0.2 x 0.04	0.4 x 0.2 x 0.08
radiation	MoK α (λ = 0.71073 Å)	
ϑ range / °	2.617–25.680	2.619–26.020
limiting indices	-57 < <i>h</i> < 57 -10 < <i>k</i> < 10 -11 < <i>l</i> < 11	-58 < <i>h</i> < 58 -11 < <i>k</i> < 11 -11 < <i>l</i> < 12
reflections collected	21644	20832
unique reflections	7666	7958
data/restraints/parameters	7666/239/681	7958/342/683
<i>R</i>_{int}	0.0443	0.0468
completeness / %	99.8	99.8
Flack parameter	0.025(8)	0.024(8)
GOF on <i>F</i>²	1.191	1.123
final <i>R</i> indices	<i>R</i> ₁ = 0.0477 [<i>I</i> > 2 σ (<i>I</i>)] <i>wR</i> ₂ = 0.0812 (all data)	<i>R</i> ₁ = 0.0456 [<i>I</i> > 2 σ (<i>I</i>)] <i>wR</i> ₂ = 0.0794 (all data)
largest diff. peak and hole / e·Å⁻³	1.333 and -2.687	1.258 and -2.863

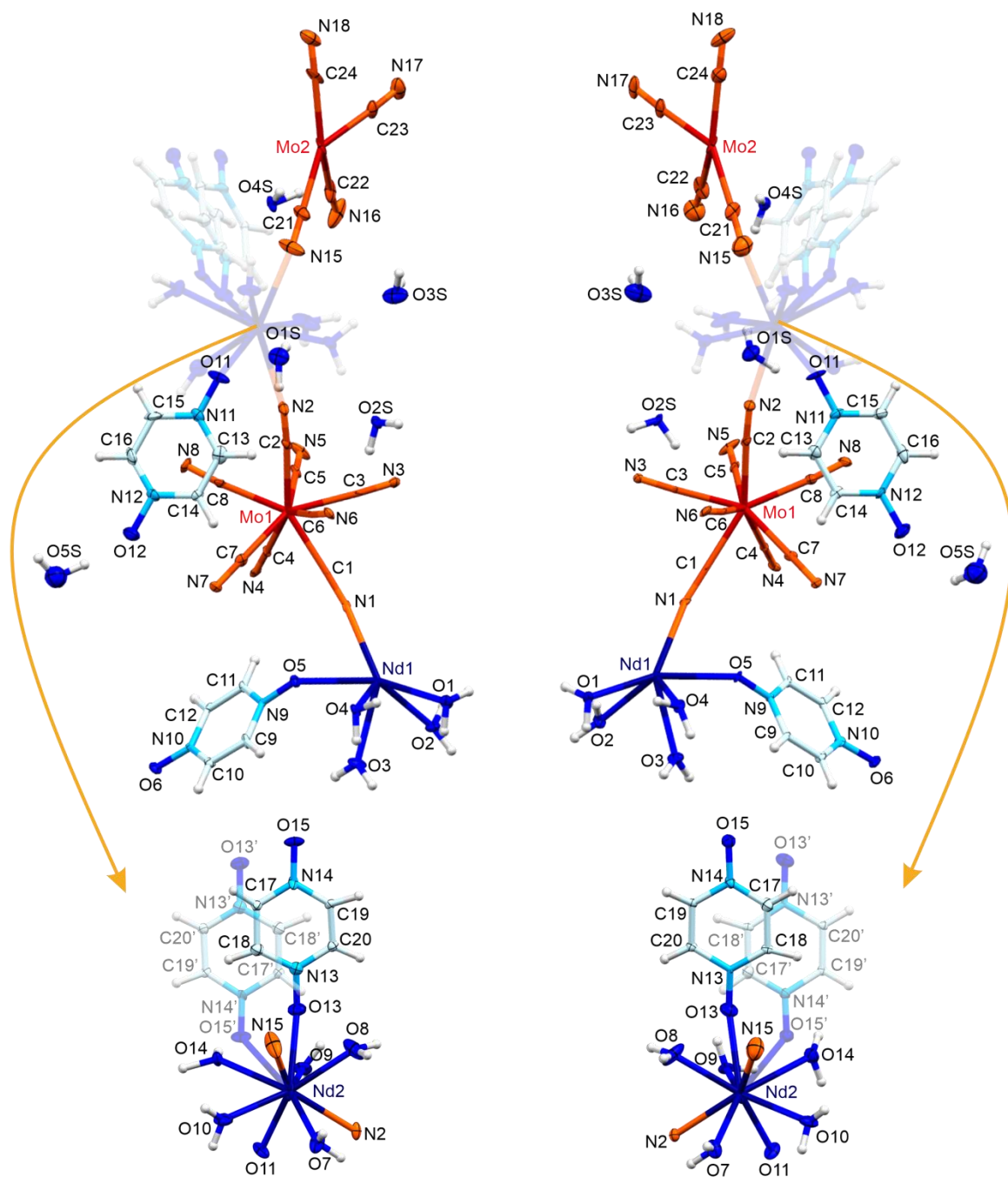


Fig. S3 The asymmetric units of **1a** (left) and **1b** (right), shown together with the enlargement of Nd2 coordination spheres. Thermal ellipsoids are presented at the 50% probability level. Hydrogen atoms were depicted as white, fixed sizes spheres with a 0.15 Å radius, while all other atoms are labelled in the figure. Note that the Nd2 complexes exist in two different forms, each of the 0.5 occupation (static structural disorder). The first version of Nd2 centre coordinates nine atoms, including O10, O11, O7, N2, N15, O8, O9, O14, and O13, while the second version of Nd2 centre (named Nd2', please compare with Fig. 1) coordinates eight atoms, including seven identical with the first version (O10, O11, O7, N2, N15, O8, and O9) together with the unique O15 atom (distinguished in the figure as O15').

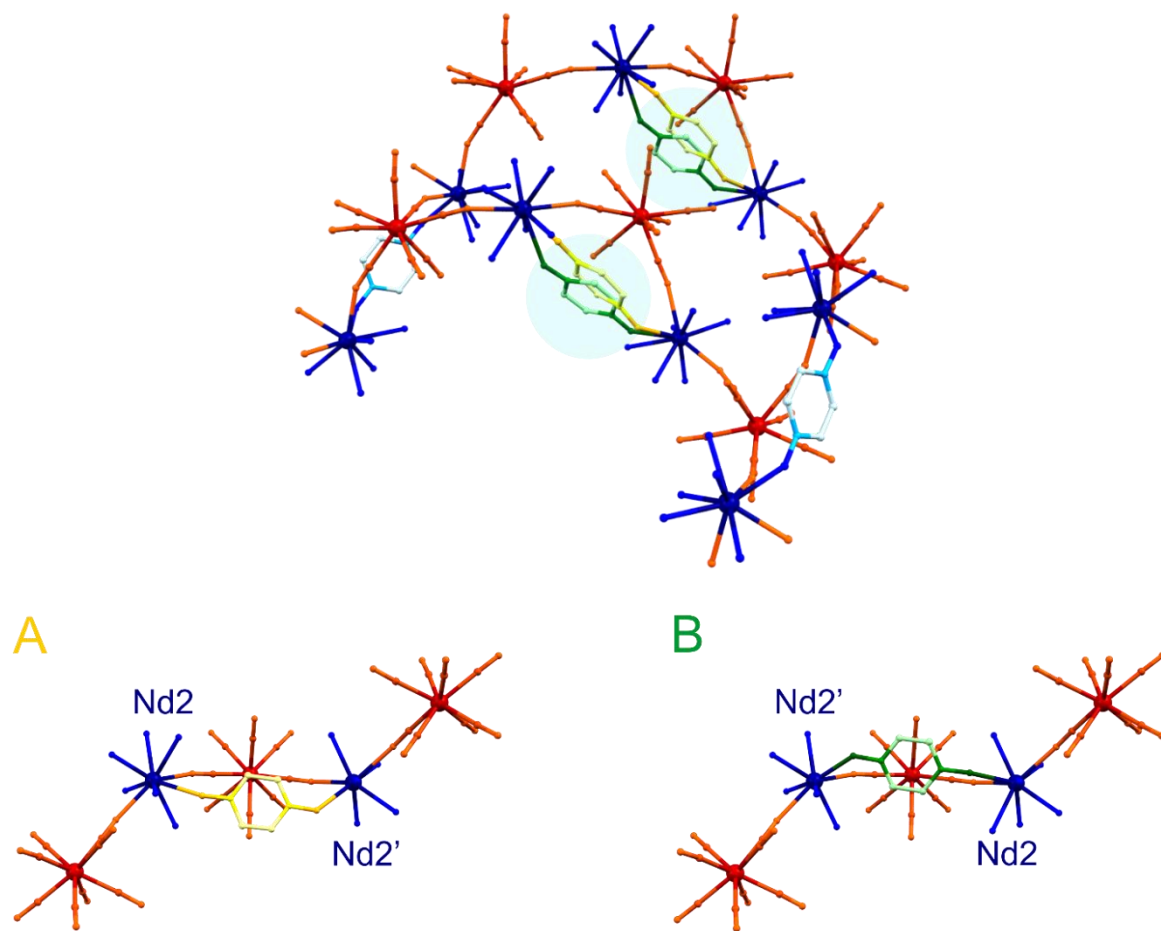


Fig. S4 Graphical presentation of the static structural disorder in **1** (shown on the example of **1b**) related to the alignment bridging pzdo ligands between Nd2 and Nd2' centres. The colour code is identical to Fig. S3 with the exception of indicated pzdo molecular bridges existing in two different positions (A and B), each of the 0.5 occupation.

Table S2 Results of Continuous Shape Measure (CShM) analysis for Mo^{IV} and Nd^{III} complexes in **1a** and **1b**. The CShM parameters are described below the table. The green colour indicates the determined coordination geometry.

Complex: [Mo(CN)₈]⁴⁻

Mo1	SAPR-8	TDD-8	BTPR-8
1a	0.279	2.185	1.877
1b	0.265	2.217	1.929

Mo2	SAPR-8	TDD-8	BTPR-8
1a	0.162	1.993	1.617
1b	0.173	2.032	1.635

Complex: [Nd(H₂O)₄(pzdo)₂(NC)₃]

Nd1	TCTPR-9	CSAPR-9	CCU-9	HBPY-9
1a	0.189	0.851	10.190	21.158
1b	0.200	0.884	10.051	20.962

Complex: [Nd(H₂O)₅(pzdo)₂(NC)₂]⁺

Nd2	TCTPR-9	CSAPR-9	CCU-9	HBPY-9
1a	0.906	0.766	8.308	19.516
1b	0.915	0.712	8.258	19.445

Complex: [Nd(H₂O)₄(pzdo)₂(NC)₂]⁺

Nd2'	SAPR-8	TDD-8	BTPR-8
1a	3.252	1.158	2.300
1b	3.334	1.208	2.399

CShM parameters:

SAPR-8 Square antiprism geometry (*D*_{4d} symmetry)

TDD-8 Triangular dodecahedron geometry (*D*_{2d} symmetry)

BTPR-8 Biaugmented trigonal prism geometry (*C*_{2v} symmetry)

HBPY-9 Heptagonal bipyramid (*D*_{7h} symmetry)

CCU-9 Capped cube (*C*_{4v} symmetry)

CSAPR-9 Capped square antiprism (*C*_{4v} symmetry)

TCTPR-9 Tricapped trigonal prism (*D*_{3h} symmetry)

CShM = 0 for the ideal geometry; the increase of a CShM parameter indicates the growing distortion from an ideal polyhedron.

References: (a) M. Llunell, D. Casanova, J. Cirera, J. Bofill, P. Alemany, S. Alvarez, M. Pinsky and D. Avnir, *SHAPE v. 2.1. Program for the Calculation of Continuous Shape Measures of Polygonal and Polyhedral Molecular Fragments*, University of Barcelona: Barcelona, Spain, 2013; (b) D. Casanova, J. Cirera, M. Llunell, P. Alemany, D. Avnir and S. Alvarez, *J. Am. Chem. Soc.*, 2004, **126**, 1755.

Table S3 Detailed structural parameters of Nd1 and Nd2 complexes in **1a** and **1b**.

Nd1 centre	1a	1b	Nd2 centre	1a	1b
Nd1-O1	2.528(10) Å	2.528(9) Å	Nd2-O7	2.448(11) Å	2.448(10) Å
Nd1-O2	2.550(8) Å	2.565(7) Å	Nd2-O8	2.440(11) Å	2.431(10) Å
Nd1-O3	2.528(10) Å	2.526(10) Å	Nd2-O9	2.539(9) Å	2.541(9) Å
Nd1-O4	2.524(7) Å	2.513(7) Å	Nd2-O10	2.445(10) Å	2.448(9) Å
Nd1-O5	2.461(10) Å	2.460(9) Å	Nd2-O11	2.433(9) Å	2.440(8) Å
Nd1-O6	2.480(10) Å	2.486(9) Å	Nd2-O13	2.629(19) Å	2.616(18) Å
Nd1-N1	2.554(9) Å	2.559(8) Å	Nd2-O14	2.643(17) Å	2.622(17) Å
Nd1-N3	2.546(12) Å	2.540(11) Å	Nd2-O15	2.29(2) Å	2.271(17) Å
Nd1-N4	2.549(12) Å	2.525(11) Å	Nd2-N2	2.574(12) Å	2.565(11) Å
O1-Nd1-O2	70.2(3)°	70.2(3)°	Nd2-N15	2.582(14) Å	2.571(15) Å
O1-Nd1-O3	88.0(3)°	87.9(3)°	O7-Nd2-O8	82.8(4)°	82.8(4)°
O1-Nd1-O4	68.5(3)°	68.6(3)°	O7-Nd2-O9	140.1(3)°	139.6(3)°
O1-Nd1-O5	140.6(3)°	141.0(3)°	O7-Nd2-O10	76.6(3)°	76.7(3)°
O1-Nd1-O6	74.2(3)°	74.4(3)°	O7-Nd2-O11	90.6(3)°	90.5(3)°
O1-Nd1-N1	134.5(4)°	134.2(4)°	O7-Nd2-O13	142.5(5)°	141.5(5)°
O1-Nd1-N3	136.8(3)°	136.4(3)°	O7-Nd2-O14	142.7(4)°	143.0(5)°
O1-Nd1-N4	72.8(3)°	72.8(3)°	O7-Nd2-O15	147.2(5)°	147.6(5)°
O2-Nd1-O3	67.9(3)°	67.7(3)°	O7-Nd2-N2	71.1(4)°	71.1(3)°
O2-Nd1-O4	118.7(2)°	118.8(2)°	O7-Nd2-N15	82.3(5)°	82.5(4)°
O2-Nd1-O5	130.8(3)°	130.4(3)°	O8-Nd2-O9	89.8(3)°	90.0(3)°
O2-Nd1-O6	133.5(4)°	133.8(3)°	O8-Nd2-O10	138.5(4)°	138.9(3)°
O2-Nd1-N1	120.1(3)°	119.3(3)°	O8-Nd2-O11	146.8(3)°	147.1(3)°
O2-Nd1-N3	66.6(3)°	66.1(3)°	O8-Nd2-O13	61.4(5)°	60.5(5)°
O2-Nd1-N4	68.0(3)°	67.5(3)°	O8-Nd2-O14	126.4(5)°	125.7(5)°
O3-Nd1-O4	67.3(3)°	67.5(3)°	O8-Nd2-O15	102.1(6)°	101.7(5)°
O3-Nd1-O5	75.3(3)°	75.5(3)°	O8-Nd2-N2	73.6(4)°	73.5(4)°
O3-Nd1-O6	139.5(3)°	139.6(3)°	O8-Nd2-N15	69.6(4)°	69.8(3)°
O3-Nd1-N1	137.5(4)°	137.9(4)°	O9-Nd2-O10	128.4(3)°	128.1(3)°
O3-Nd1-N3	75.7(3)°	75.3(3)°	O9-Nd2-O11	74.6(3)°	74.5(3)°
O3-Nd1-N4	135.7(3)°	134.9(3)°	O9-Nd2-O13	56.3(5)°	57.5(5)°
O4-Nd1-O5	72.1(3)°	72.4(3)°	O9-Nd2-O14	70.1(5)°	70.3(5)°
O4-Nd1-O6	72.3(3)°	72.3(3)°	O9-Nd2-O15	72.7(5)°	72.7(5)°
O4-Nd1-N1	121.3(2)°	121.9(2)°	O9-Nd2-N2	69.2(4)°	68.7(3)°
O4-Nd1-N3	134.5(4)°	134.3(4)°	O9-Nd2-N15	131.3(5)°	131.7(4)°
O4-Nd1-N4	133.8(4)°	134.1(3)°	O10-Nd2-O11	69.6(3)°	68.9(3)°
O5-Nd1-O6	95.7(2)°	95.7(2)°	O10-Nd2-O13	122.6(5)°	123.1(5)°
O5-Nd1-N1	69.9(3)°	70.4(3)°	O10-Nd2-O14	66.1(5)°	66.3(5)°

Nd1 centre	1a	1b	Nd2 centre	1a	1b
O5-Nd1-N3	73.6(3)°	73.4(3)°	O10-Nd2-O15	78.8(5)°	79.5(5)°
O5-Nd1-N4	141.8(3)°	141.8(3)°	O10-Nd2-N2	130.0(4)°	129.8(3)°
O6-Nd1-N1	68.9(3)°	68.9(3)°	O10-Nd2-N15	72.2(4)°	72.5(4)°
O6-Nd1-N3	140.4(3)°	140.7(3)°	O11-Nd2-O13	125.3(5)°	126.4(5)°
O6-Nd1-N4	73.6(3)°	74.2(3)°	O11-Nd2-O14	76.0(5)°	76.7(5)°
Nd1-N1-C1 (CN ⁻)	160.6(8)°	159.4(8)°	O11-Nd2-O15	100.9(5)°	101.1(5)°
Nd1-N3-C3 (CN ⁻)	156.9(10)°	157.7(9)°	O11-Nd2-N2	73.6(3)°	73.8(3)°
Nd1-N4-C4 (CN ⁻)	157.6(10)°	157.6(9)°	O11-Nd2-N15	141.8(3)°	141.4(3)°
Nd1-O5-N9 (pzdo)	136.6(7)°	137.3(6)°	O13-Nd2-O14	66.3(6)°	66.4(6)°
Nd1-O6-N10 (pzdo)	134.6(8)°	133.0(7)°	O13-Nd2-N2	106.1(5)°	105.9(5)°
			O13-Nd2-N15	75.3(6)°	74.6(5)°
			O14-Nd2-N2	134.1(5)°	134.4(5)°
			O14-Nd2-N15	87.2(6)°	86.4(5)°
			O15-Nd2-N2	141.7(5)°	141.1(5)°
			O15-Nd2-N15	69.6(6)°	69.5(6)°
			Nd2-N2-C2 (CN ⁻)	165.0(12)°	164.8(10)°
			Nd2-N15-C21 (CN ⁻)	161.7(15)°	161.6(14)°
			Nd2-O11-N11 (pzdo)	131.9(7)°	131.1(7)°
			Nd2-O13-N13 (pzdo)	140.7(17)°	143.3(15)°
			Nd2-O15-N14 (pzdo)	132.6(16)°	133.9(14)°

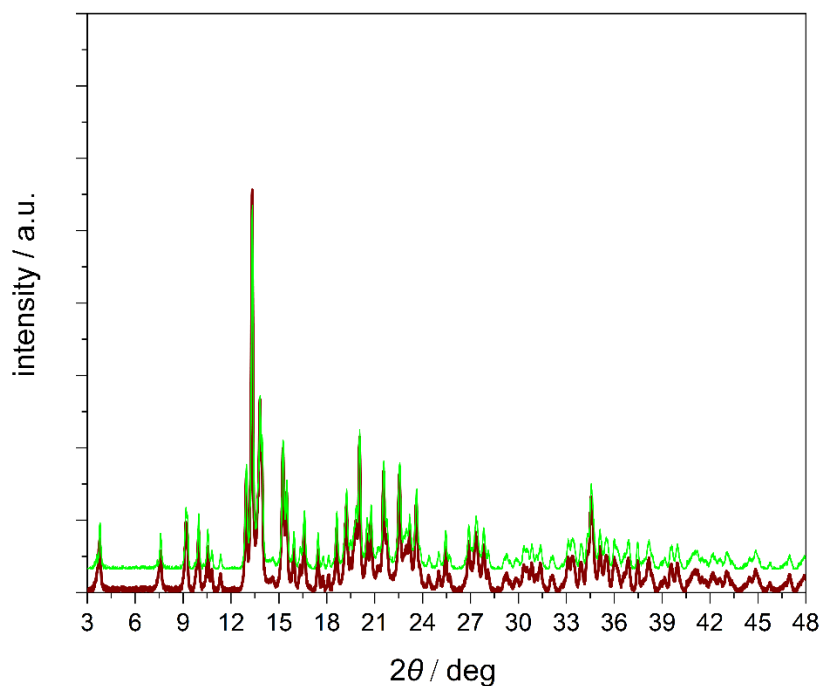


Fig. S5 Experimental powder X-ray (P-XRD) pattern of the bulk sample of **1** (dark red line) compared with the simulated P-XRD pattern (green line) obtained as a result of the LeBail fitting procedure performed using an EXPO 2014 software.

References: a) A. Altomare, C. Cuocci, C. Giacovazzo, A. Moliterni, R. Rizzi, N. Corriero and A. Falcicchio, *J. Appl. Cryst.*, 2013, **46**, 1231; b) A. Altomare, C. Giacovazzo, A. Guagliardi, A. G. G. Moliterni, R. Rizzi and P.-E. Werner, *J. Appl. Cryst.*, 2000, **33**, 1180; c) A. Boultif and D. Louër, *J. Appl. Cryst.*, 2004, **37**, 724.

Table S4 Comparison of the unit cell parameters of **1** and **2** determined using the P-XRD method for bulk samples (**1** and **2**) or the SC-XRD method for single crystals (**1a** and **1b**).

unit cell parameters	1			2
	1a (SC-XRD)	1b (SC-XRD)	1 (P-XRD)	P-XRD
$a / \text{Å}$	47.022(2)	47.052(3)	47.16(2)	47.09(3)
$b / \text{Å}$	9.0142(4)	9.0064(5)	9.008(3)	8.995(5)
$c / \text{Å}$	9.7443(4)	9.7326(5)	9.775(3)	9.765(4)
$\beta / ^\circ$	100.4000(10)	100.309(2)	100.44(3)	100.33(4)
$V / \text{Å}^3$	4062.4(3)	4057.8(4)	4084(3)	4070(4)

Table S5 The comparison of coordination topologies, coordination geometries of Ln^{III} centres, magnetic and optical properties of the selected Ln^{III}–[Mo^{IV}/W^{IV}(CN)₈]^{4–} coordination systems.

Ln ^{III} –[M ^{IV} (CN) ₈] ^{4–} system	topology (space group)	Ln ^{III} coordination geometry	magnetic properties	optical properties	citations
[Ln ^{III} (mpca) ₂ (H ₂ O) _x (CH ₃ OH) _y Ln(H ₂ O) ₆ Mo ^{IV} (CN) ₈] _n ·nH ₂ O	3-D network of I ² O ¹ connectivity, built of inorganic layers of alternating diamond-like and octahedral rings, cross-linked in the 3 rd dimension by additional Ln ^{III} complexes via mpca ligands (P2 ₁ /c)	8-coordinated square antiprismatic complexes; 9-coordinated tricapped trigonal prismatic complexes	magnetic coupling between Tb ^{III} complexes	visible light emission for Eu ^{III} and Tb ^{III} complexes	(a)
[Ln ^{III} (mpca) ₂ (H ₂ O) _x (CH ₃ OH) _y Ln(H ₂ O) ₆ W ^{IV} (CN) ₈] _n ·nH ₂ O			–	red emission for Eu ^{III} complexes sensitive to humidity level	(b)
{KH[Ln ^{III} ₂ (pzdc) ₂ (CH ₃ OH)(H ₂ O) ₇][Mo ^{IV} (CN) ₈]}·5H ₂ O	3-D network of I ² O ¹ connectivity, built of inorganic layers of octagon-like rings with K ⁺ cations, cross-linked in the 3 rd dimension by additional Ln ^{III} complexes via pzdc ligands (C2/c)	9-coordinated trigonal prismatic complexes	the onset of field-induced magnetic relaxation for Dy ^{III} complexes (U _{eff} = 12.77 K)	–	(c)
{KH[Ln ^{III} ₂ (pzdc) ₂ (CH ₃ OH)(H ₂ O) ₇][W ^{IV} (CN) ₈]}·5H ₂ O			–	–	(c)
(Hphen) _{2.5} [Ln ^{III} _{0.5} (phen)(H ₂ O)][Mo ^{IV} (CN) ₈] _{1.5} ·CH ₃ CN	0-D trinuclear cyanido-bridged anionic clusters with additional Hphen ⁺ cations (C2/c)	8-coordinated square antiprismatic complexes	the onset of field-induced magnetic relaxation for Dy ^{III} and Er ^{III} complexes	–	(d)
(PPN)[Ln ^{III} (pzdo) ₂ (CH ₃ OH) _{0.3} (H ₂ O) _{3.7}][Mo ^{IV} (CN) ₈] _{7.7} ·7H ₂ O·2CH ₃ OH	1-D anionic metal-organic chains of I ⁰ O ¹ connectivity with additional PPN ⁺ cations (P2 ₁ /c)	8-coordinated dodecahedral complexes	SMM behaviour for Yb ^{III} (U _{eff} = 26(1) K) and Er ^{III} (U _{eff} = 24(1) K)	UV-Vis induced NIR emission for Yb ^{III} complexes	(e)
(PPN)[Ln ^{III} (pzdo) ₂ (CH ₃ OH) _{0.3} (H ₂ O) _{3.7}][W ^{IV} (CN) ₈] _{7.7} ·7H ₂ O·2CH ₃ OH			SMM behaviour for Yb ^{III} (U _{eff} = 27(2) K) and Er ^{III} (U _{eff} = 24(1) K)	UV-Vis induced NIR emission for Yb ^{III} and Er ^{III} complexes	
1	2-D neutral layers of I ² O ¹ connectivity with additional local Nd ^{III} -pzdo-Nd ^{III} linkages (C2)	8-coordinated dodecahedral complexes; 9-coordinated tricapped trigonal prismatic and capped square antiprismatic complexes	SMM behaviour with U _{eff} = 8.0(3) K	UV-Vis induced NIR emission and SHG activity	this work
			SMM behaviour with U _{eff} = 5.6(5) K		

Hmpca = 5-methyl-2-pyrazine carboxylic acid; H₂pzdc = pyrazine-2,3-dicarboxylic acid; phen = 1,10-phenanthroline; pzdo = pyrazine-N,N'-dioxide.

References: (a) S. Tanase, M. C. Mittelmeijer-Hazeleger, G. Rothenberg, C. Mathonière, V. Jubera, J. M. M. Smits and R. d. Gelder, *J. Mater. Chem.*, 2011, **21**, 15544; (b) Y. Gao, P. Jing, N. Yan, M. Hilbers, H. Zhang, G. Rothenberg and S. Tanase, *Chem. Commun.*, 2017, **53**, 4465; (c) Y. Gao, M. Viciano-Chumillas, A. M. Toader, S. J. Teat, M. Ferbinteanu and S. Tanase, *Inorg. Chem. Front.*, 2018, **5**, 1967; (d) H. Zhou, Q. Chen, H.-B. Zhou, X.-Z. Yang, Y. Song and A.-H. Yuan, *Cryst. Growth Des.*, 2016, **16**, 1708; (e) R. Jankowski, J. J. Zakrzewski, O. Surma, S. Ohkoshi, S. Chorazy and B. Sieklucka, *Inorg. Chem. Front.*, 2019, **6**, 2423.

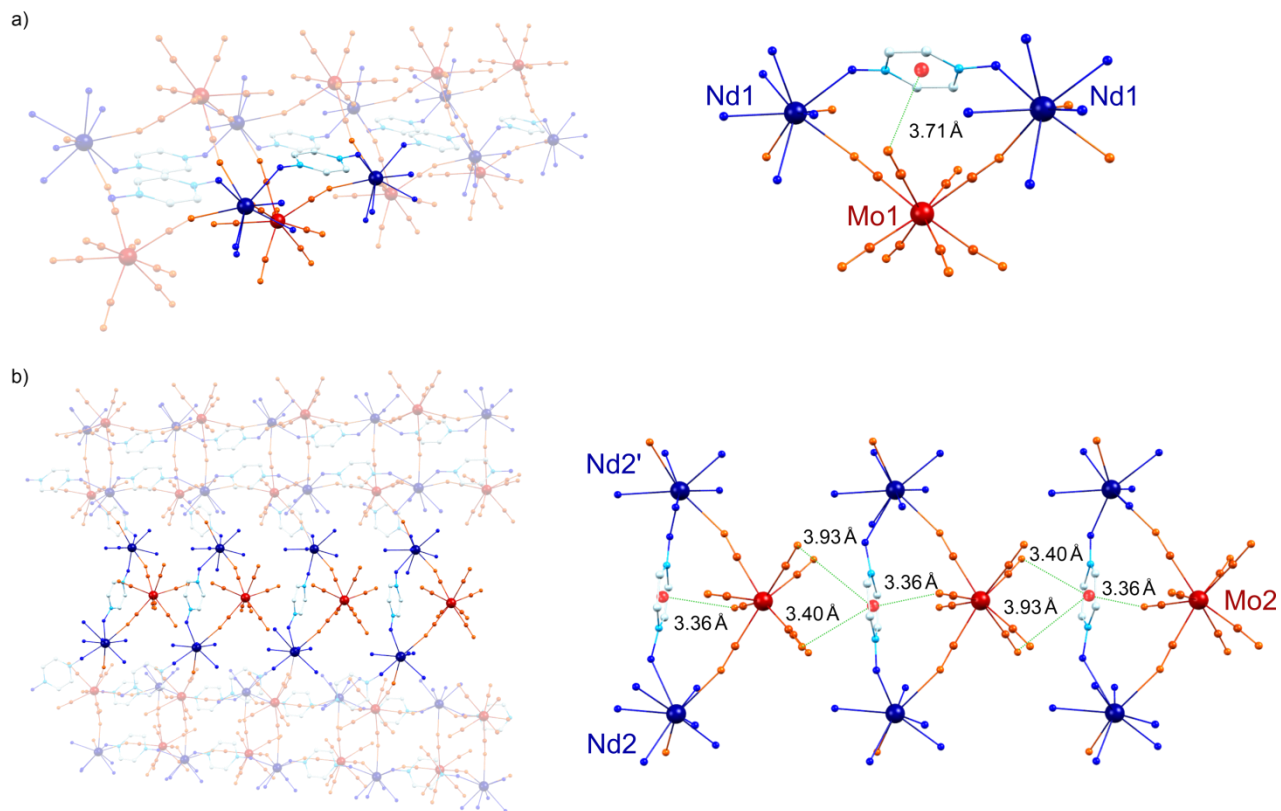


Fig. S6 Schematic representation of anion- π interactions within cyanido-bridged ladder-like fragments (a), and trinuclear $\{\text{Nd}_2\text{Mo}_1(\text{pzdo})\}$ spacers (b) in **1a**.

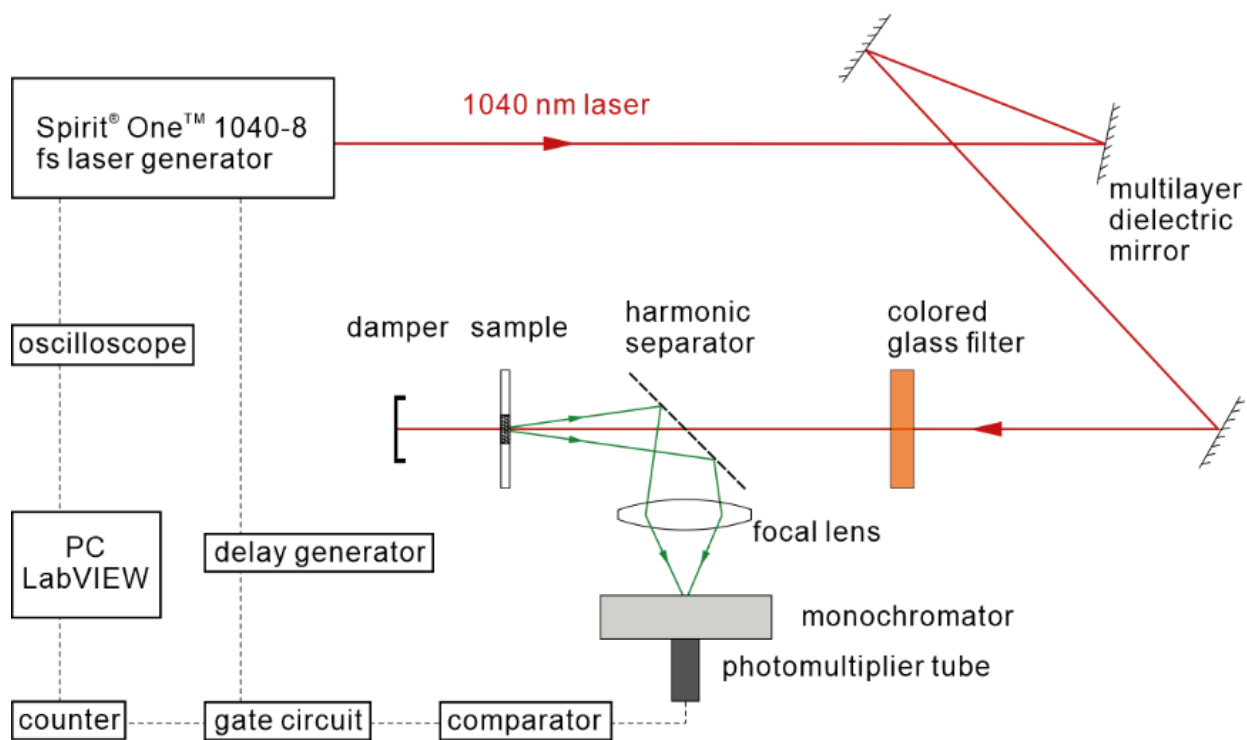


Fig. S7 The schematic presentation of the experimental setup used for SHG measurements performed for the polycrystalline samples of **1** and **2**.

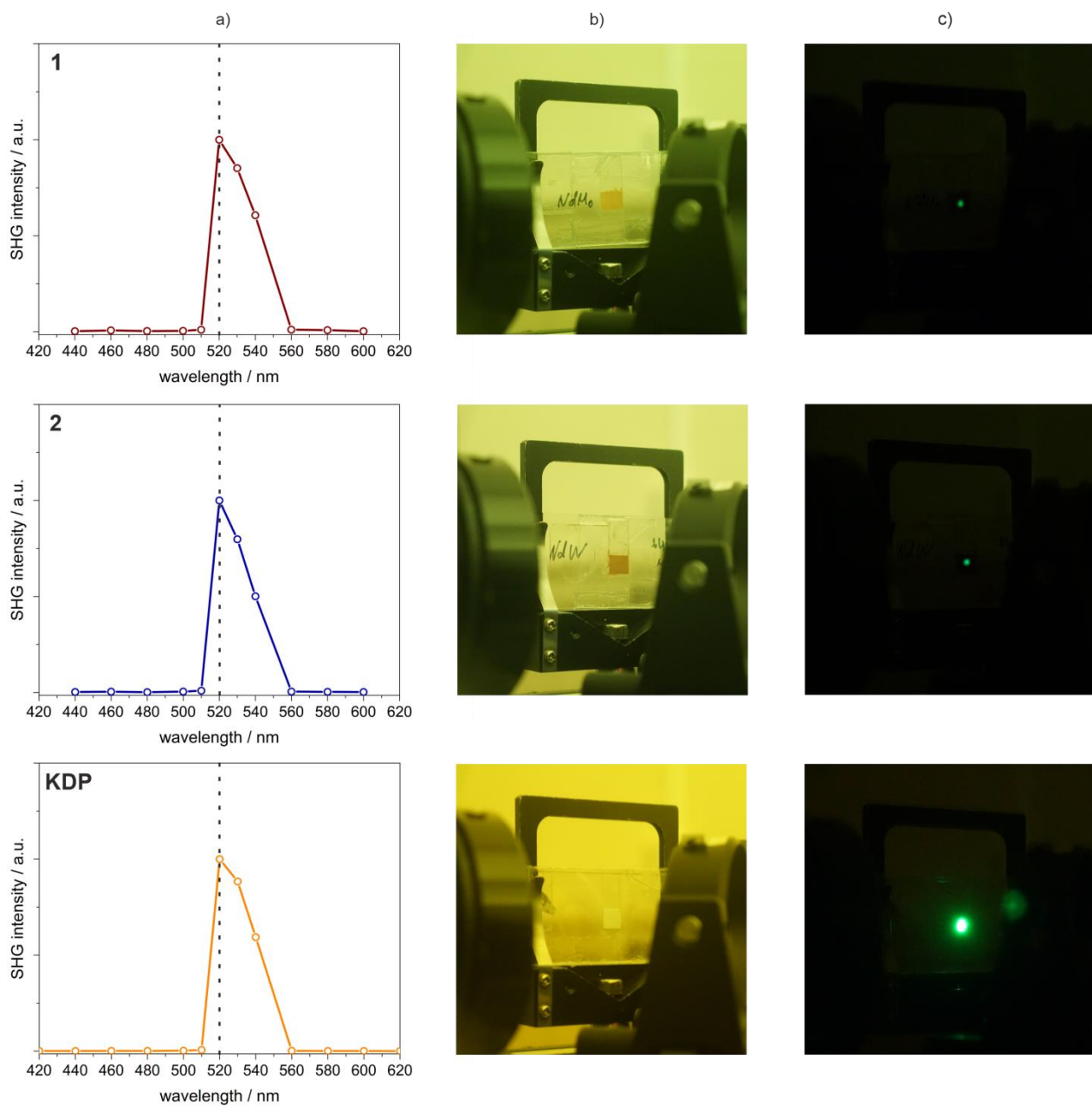


Fig. S8 Wavelength-dependences of the SH signal (a), the photos of the respective samples mounted in the SHG experimental setup (b), and the photos of the observed SH light from the respective samples under the 1040 nm laser irradiation (c) for the indicated compounds **1** (top), **2** (middle), and the reference of potassium dihydrogen phosphate (KDP) (bottom).

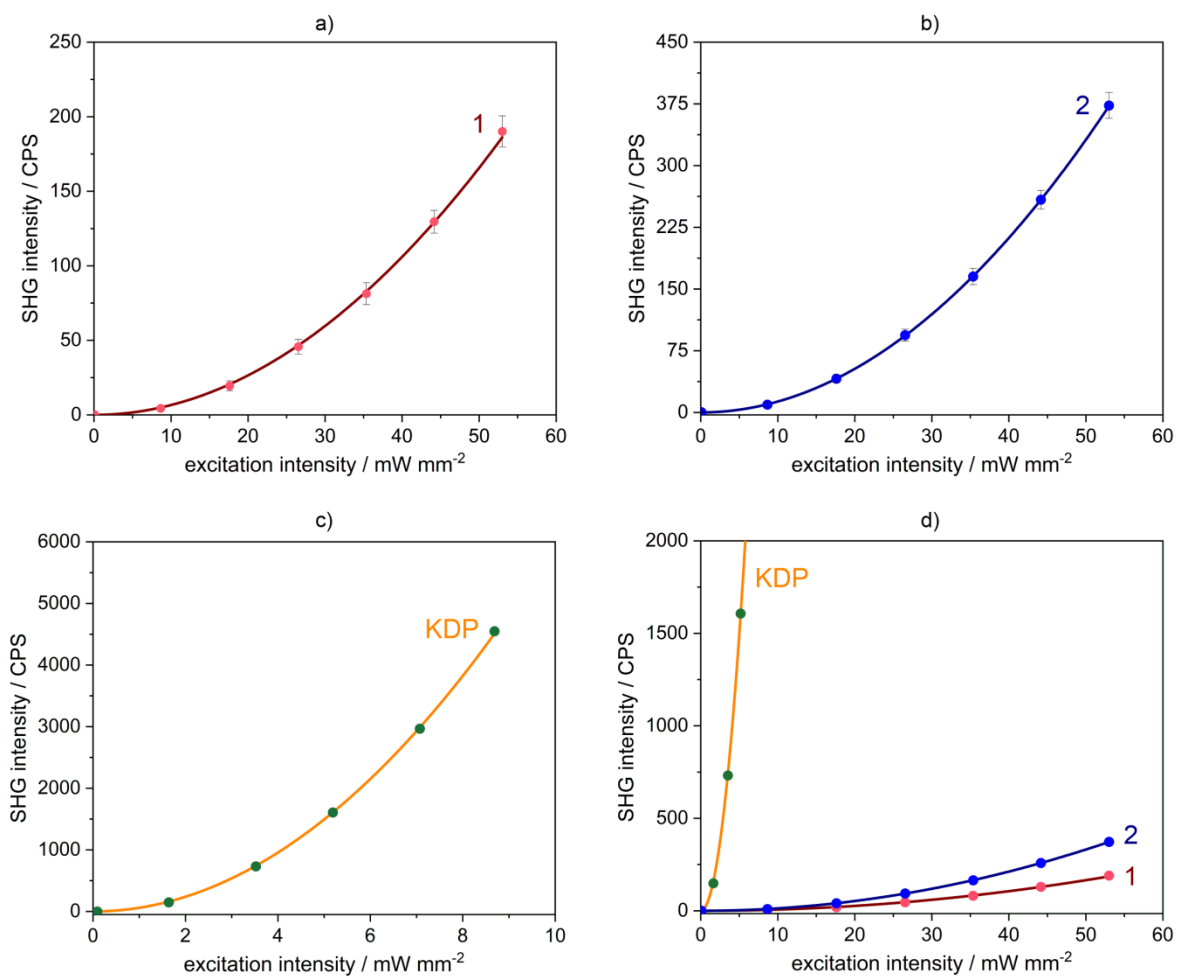


Fig. S9 Dependences of the SH light intensity on the excitation light intensity for the powder samples **1** (a), **2** (b), and the referential material of KDP (c), together with the comparison of the respective SH intensities for all measured samples (d). Coloured points represent the experimental results while the solid lines represent the best-fit curves according to the quadratic function indicating the SH nature of detected light.

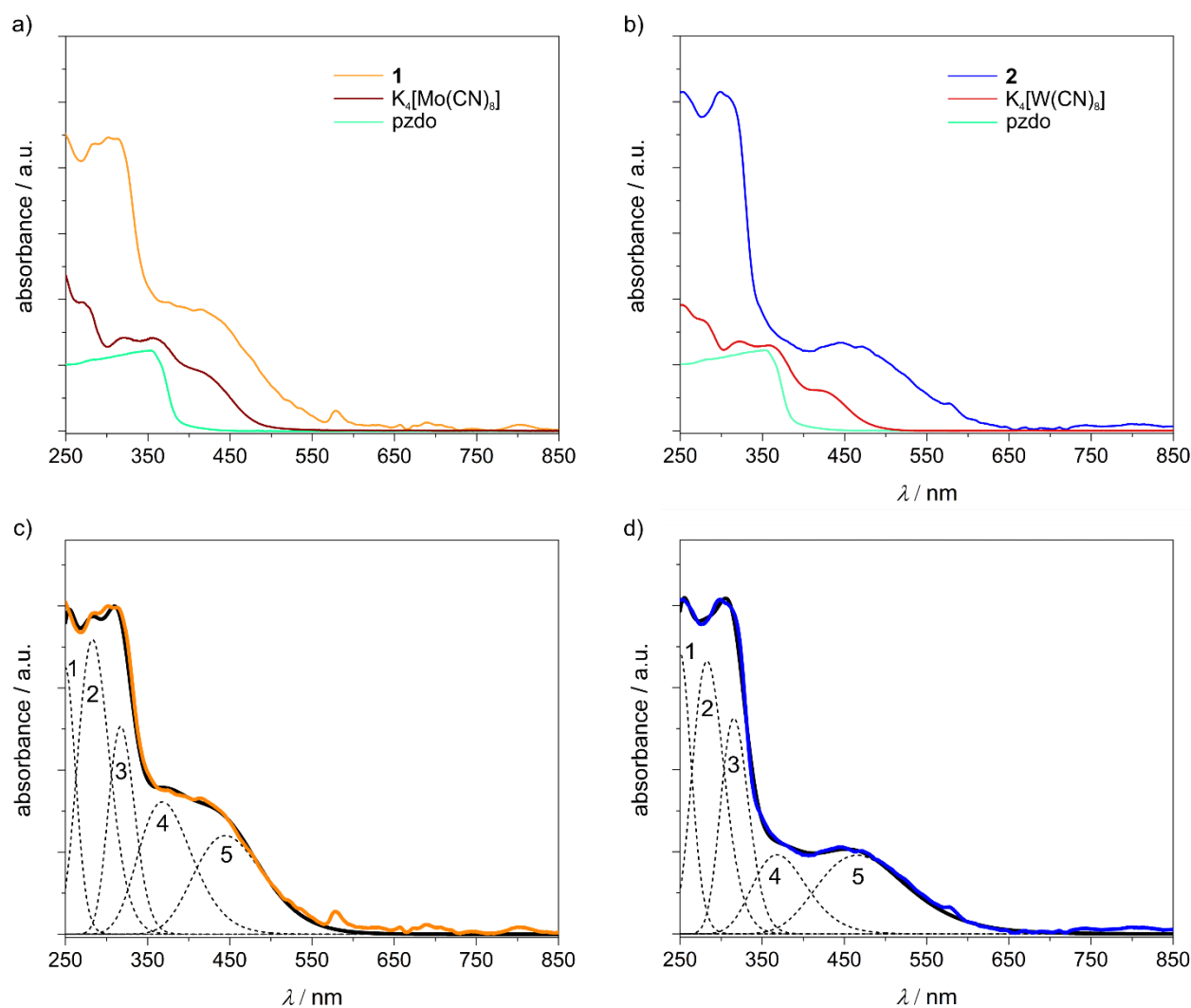


Fig. S10 Solid-state UV-vis absorption spectra for **1** (a) and **2** (b), compared with the reference spectra of the respective octacyanidometallate(IV) salts and organic pzdo ligand, and the absorption spectra of **1** (c) and **2** (d) shown together with the results of deconvolution of broad UV-to-vis patterns into five Gaussian components (see Table S6). In (c) and (d), coloured solid lines represent the experimental data, black lines show the sum of five absorption components obtained in the deconvolution process. All components (1–5) originating from the deconvolution are labelled and presented by dotted black lines.

Table S6 Results of the deconvolution carried out for the solid-state absorption spectra of **1** and **2** (Fig. S10c,d).

absorption band	1 (Fig. S10c)	2 (Fig. S10d)
1	40000 cm ⁻¹ (ca. 250 nm)	40000 cm ⁻¹ (ca. 250 nm)
2	35211 cm ⁻¹ (ca. 284 nm)	35461 cm ⁻¹ (ca. 282 nm)
3	31446 cm ⁻¹ (ca. 318 nm)	31746 cm ⁻¹ (ca. 315 nm)
4	27174 cm ⁻¹ (ca. 368 nm)	27174 cm ⁻¹ (ca. 368 nm)
5	22573 cm ⁻¹ (ca. 443 nm)	21505 cm ⁻¹ (ca. 465 nm)

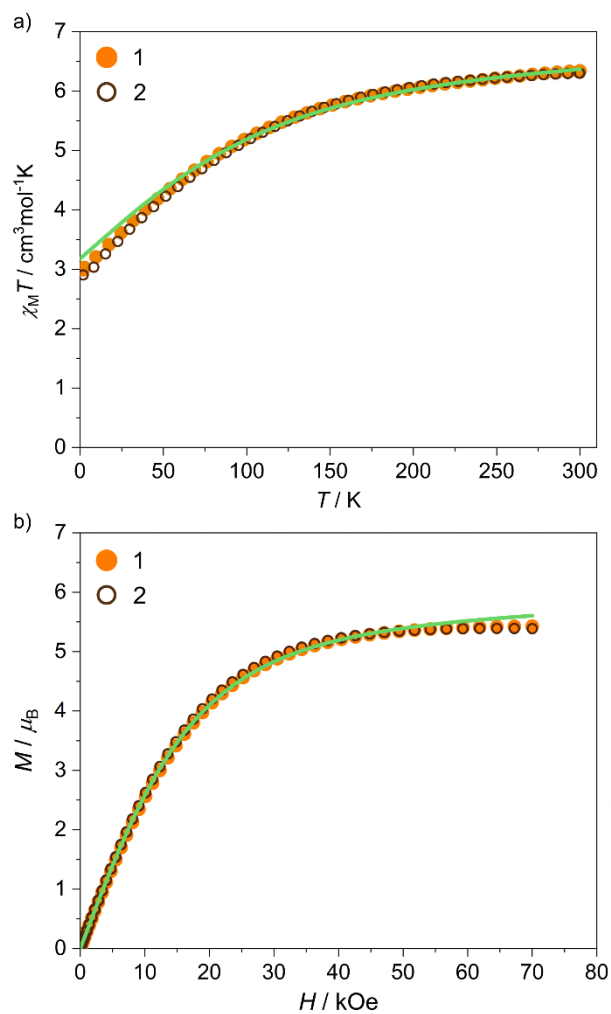


Fig. S11 Direct-current (*dc*) magnetic characteristics of **1** and **2**: the temperature dependence of the $\chi_M T$ product at $H_{\text{dc}} = 1000$ Oe (*a*) and the field dependence of molar magnetization at 1.8 K (*b*). The green lines, shown both in (*a*) and (*b*), represent the respective magnetic curves calculated from the results of *ab initio* calculations performed using the structural data of **1a** with the large basis set (Table S7) leading to the crystal-field parameters gathered in Tables S11–S13.

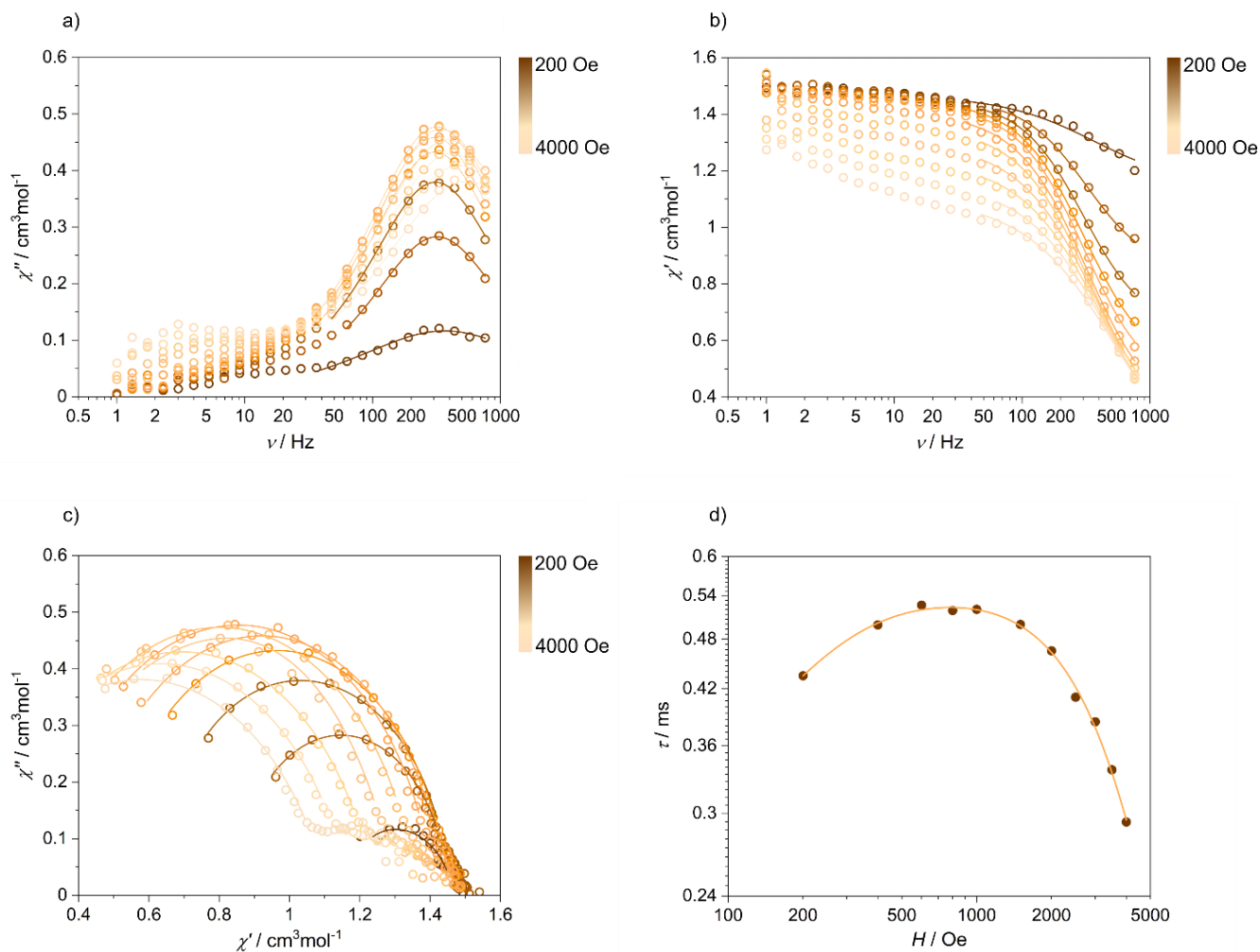


Fig. S12 Complete magnetic-field-variable alternate-current (*ac*) magnetic susceptibility characteristics of **1** gathered under $H_{ac} = 3$ Oe and $T = 1.8$ K: frequency dependences of the out-of-phase magnetic susceptibility, χ'' (a), and the in-phase magnetic susceptibility, χ' (b), both at various values of *dc* external magnetic fields, the related Argand plots (c), and the resulting field dependence of magnetic relaxation time, τ , presented in the log-log scale (d). Coloured solid lines in (a), (b), and (c) represent the best-fits based on the generalized Debye model for a single relaxation process (see comment on page S22). The solid line in (d) represents the best-fit considering three different relaxation processes: a QTM, a field-induced direct process, and a two-phonon Raman relaxation process (see equation (1) in the main text for comparison).

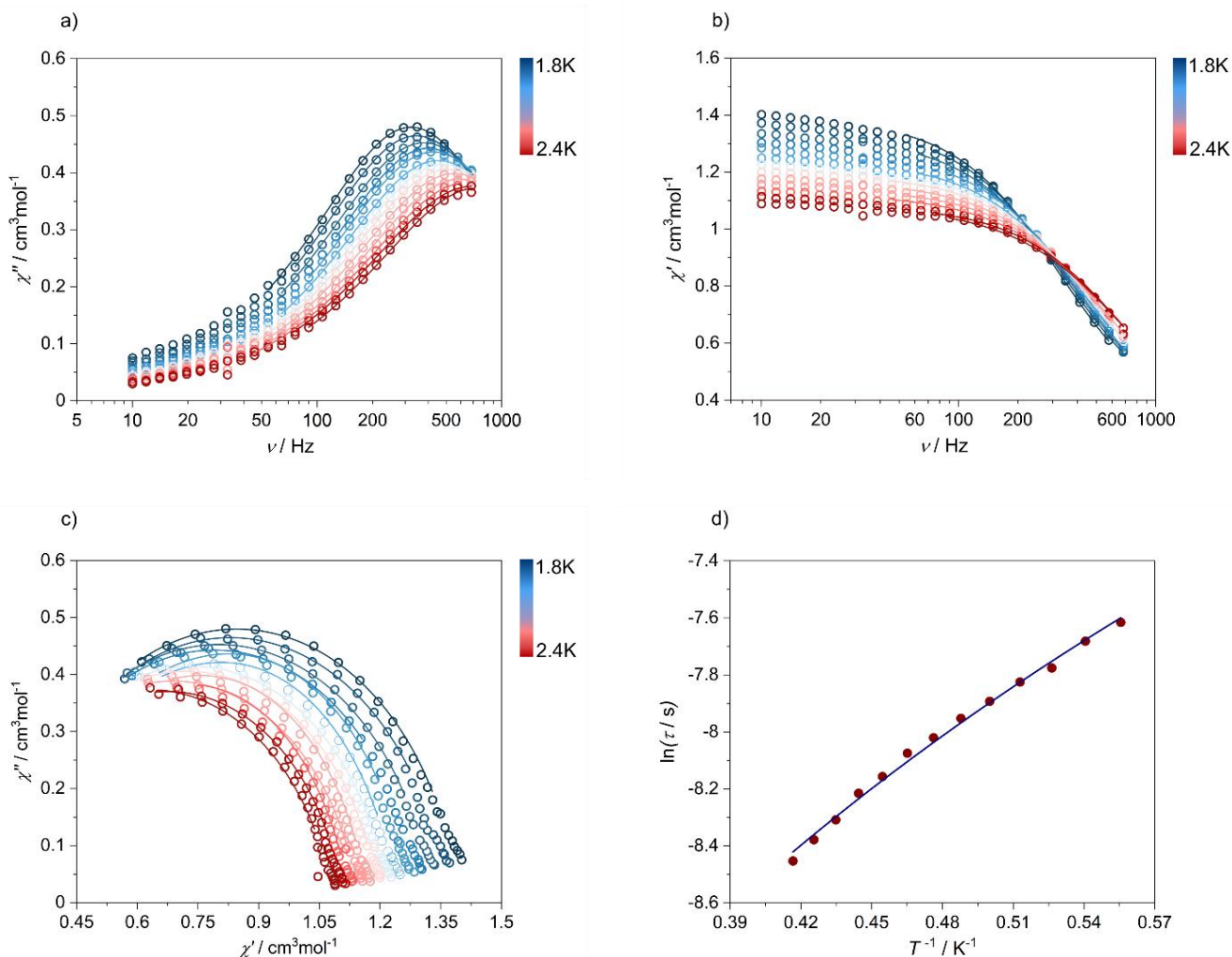


Fig. S13 Complete temperature-variable alternate-current (*ac*) magnetic susceptibility characteristics of **1** collected under $H_{ac} = 3$ Oe and $H_{dc} = 1500$ Oe: frequency dependences of the out-of-phase magnetic susceptibility, χ'' (a), and the in-phase magnetic susceptibility, χ' (b), both at various temperatures, the related Argand plots (c), and the resulting temperature dependence of magnetic relaxation time, τ (d). Coloured solid lines in (a), (b), and (c) represent the best-fits based on the generalized Debye model for a single relaxation process (see comment on page S22). The solid line in (d) represents the best-fit considering three different relaxation processes: a QTM, a field-induced direct process, and a two-phonon Raman relaxation process (see equation (1) in the main text for comparison).

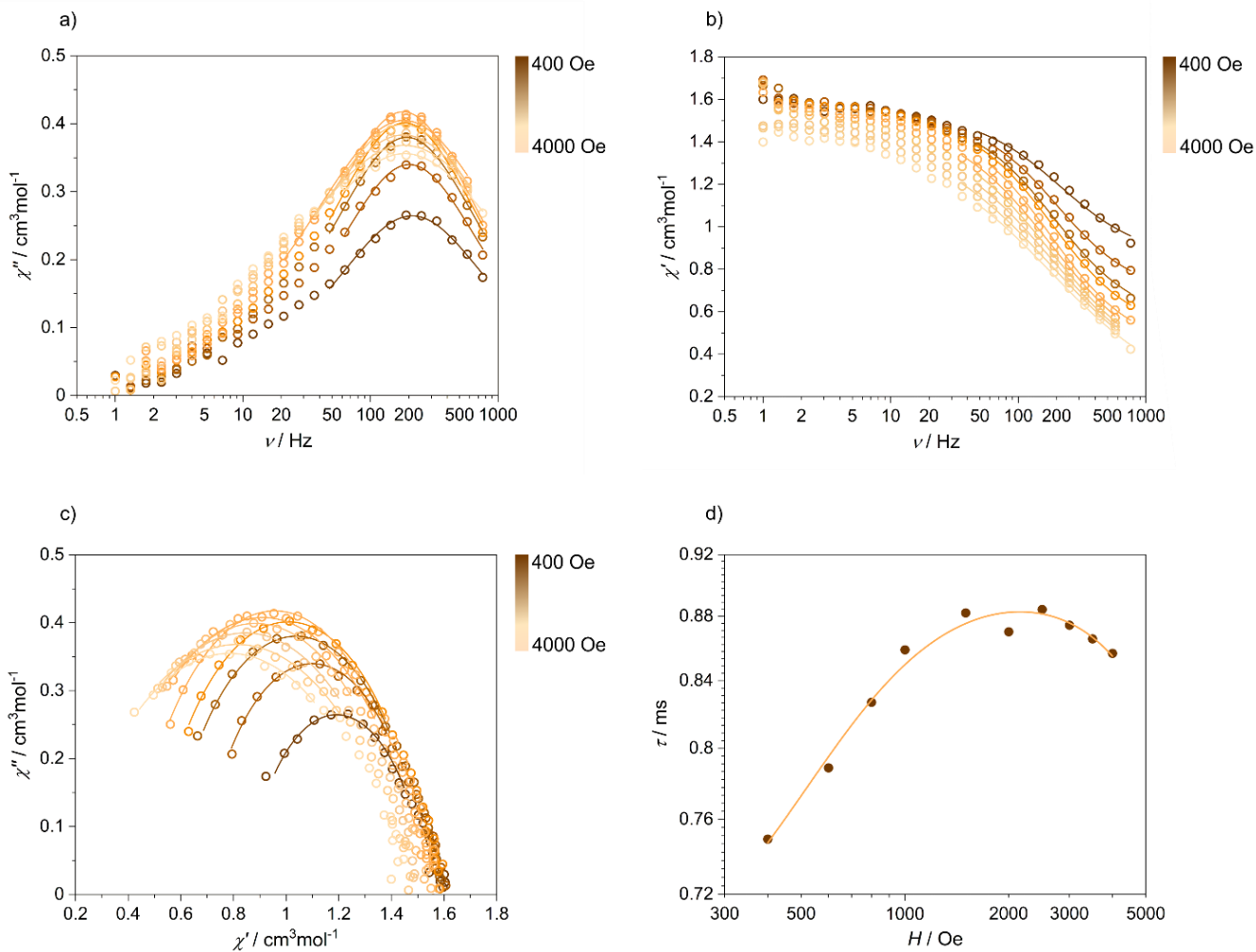


Fig. S14 Complete magnetic-field-variable alternate-current (*ac*) magnetic susceptibility characteristics of **2** gathered under $H_{ac} = 3$ Oe and $T = 1.8$ K: frequency dependences of the out-of-phase magnetic susceptibility, χ'' (a), and the in-phase magnetic susceptibility, χ' (b), both at various values of *dc* external magnetic fields, the related Argand plots (c), and the resulting field dependence of magnetic relaxation time, τ , presented in the log-log scale (d). Coloured solid lines in (a), (b), and (c) represent the best-fits based on the generalized Debye model for a single relaxation process (see comment on page S22). The solid line in (d) represents the best-fit considering three different relaxation processes: a QTM, a field-induced direct process, and a two-phonon Raman relaxation process (see equation (1) in the main text for comparison).

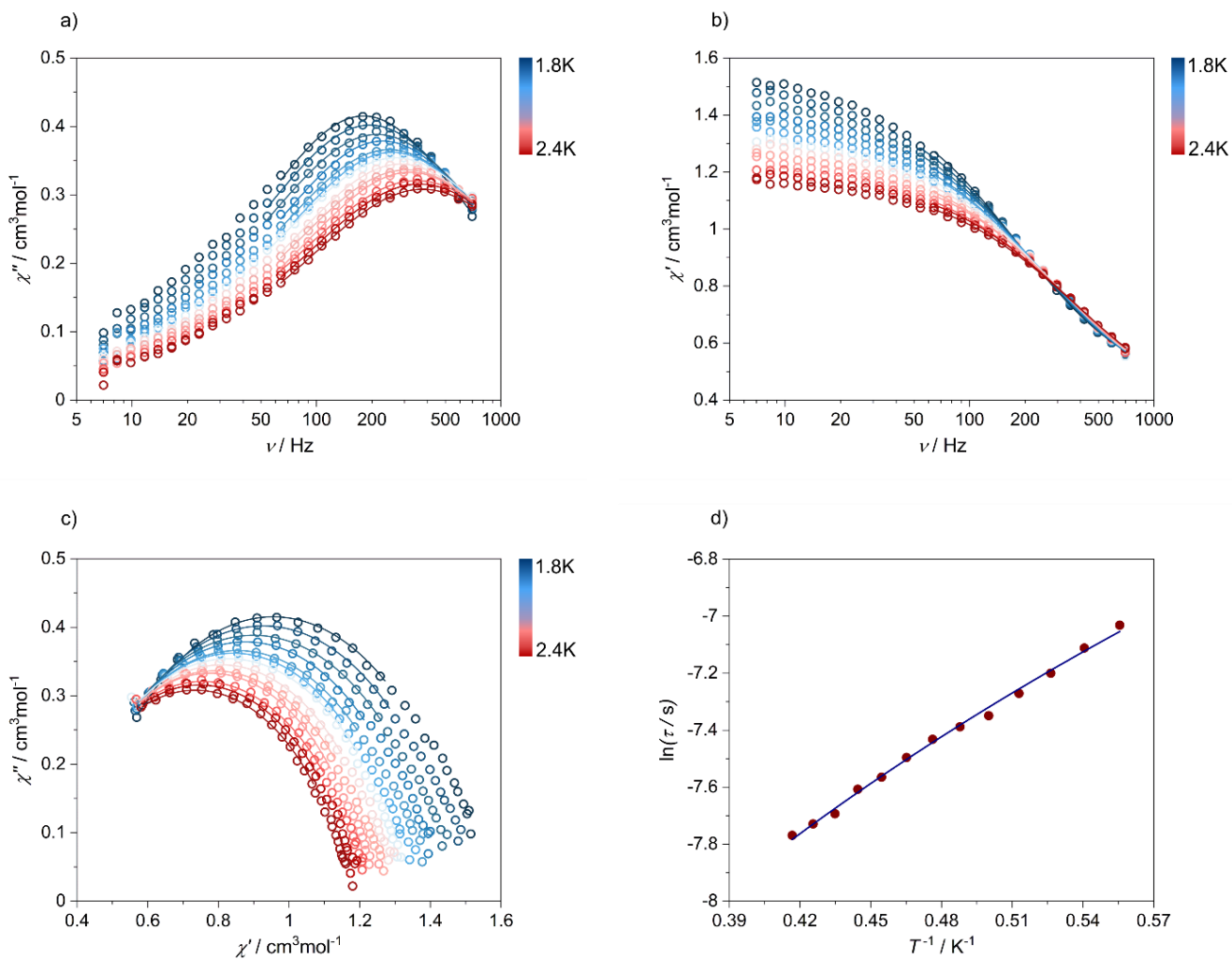


Fig. S15 Complete temperature-variable alternate-current (*ac*) magnetic susceptibility characteristics of **2** collected under $H_{ac} = 3$ Oe and $H_{dc} = 1500$ Oe: frequency dependences of the out-of-phase magnetic susceptibility, χ'' (a), and the in-phase magnetic susceptibility, χ' (b), both at various temperatures, the related Argand plots (c), and the resulting temperature dependence of magnetic relaxation time, τ (d). Coloured solid lines in (a), (b), and (c) represent the best-fits based on the generalized Debye model for a single relaxation process (see comment on page S22). The solid line in (d) represents the best-fit considering three different relaxation processes: a QTM, a field-induced direct process, and a two-phonon Raman relaxation process (see equation (1) in the main text for comparison).

Comment to Fig. S12–S15

For fitting of the frequency dependences of the χ' and χ'' contributions to the ac magnetic susceptibility, and fitting of the related Argand $\chi''(\chi')$ plots, the following equations (s1 and s2) of the generalized Debye model for a single relaxation process were applied:

$$\chi'(\omega) = \chi_S + (\chi_T - \chi_S) \frac{1 + (\omega\tau)^{1-\alpha} \sin(\pi\alpha/2)}{1 + 2(\omega\tau)^{1-\alpha} \sin(\pi\alpha/2) + (\omega\tau)^{2(1-\alpha)}} \quad (\text{s1})$$

$$\chi''(\omega) = (\chi_T - \chi_S) \frac{(\omega\tau)^{1-\alpha} \cos(\pi\alpha/2)}{1 + 2(\omega\tau)^{1-\alpha} \sin(\pi\alpha/2) + (\omega\tau)^{2(1-\alpha)}} \quad (\text{s2})$$

where

χ_S is an adiabatic susceptibility (at the infinitely high frequency of ac field),

χ_T is an isothermal susceptibility (at the infinitely low frequency of ac field),

τ stands for the relaxation time,

α stands for the distribution (Cole-Cole) parameter,

and ω is an angular frequency, that is $\omega = 2\pi\nu$, with ν being for the linear frequency in [Hz] units.

Reference: Y.-N. Guo, G.-F. Xu, Y. Guo and J. Tang, *Dalton Trans.*, 2011, **40**, 9956.

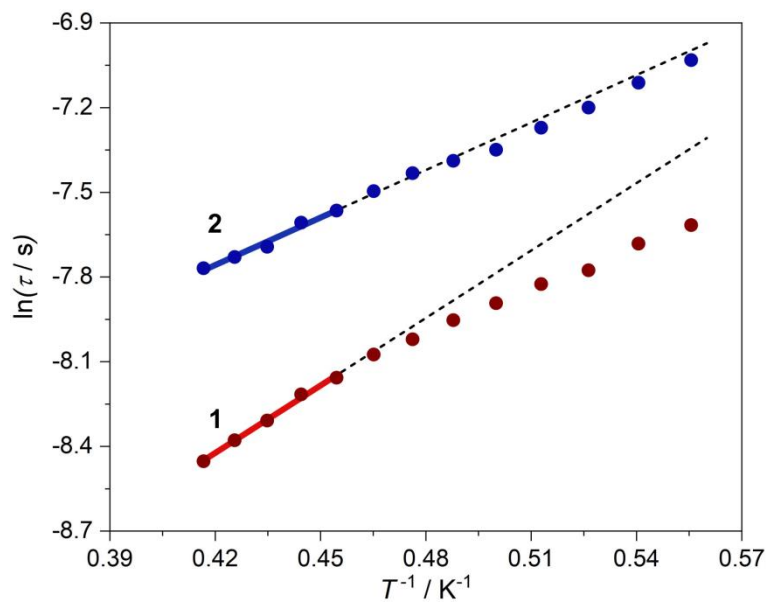


Fig. S16 Temperature dependences of magnetic relaxation time for **1** (red circles) and **2** (blue circles) shown together with the fitting of the limited high temperature range to the Arrhenius law (coloured solid lines). The black dotted lines represent the extrapolation of the best-fit curves toward lower temperatures.

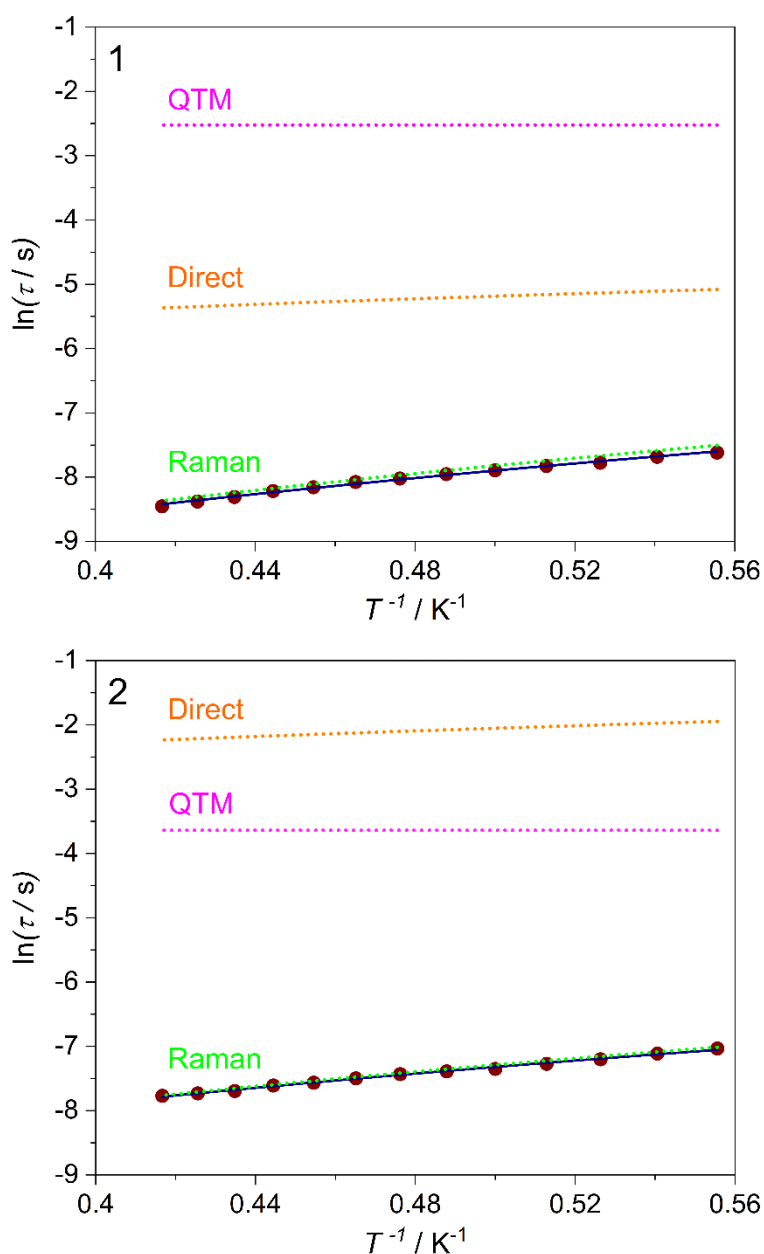


Fig. S17 Temperature dependences of magnetic relaxation time for **1** (top) and **2** (bottom) obtained from the ac measurements at the optimal dc field of 1500 Oe (Fig. S13 and S15). Red circles represent the experimental data while the dark blue solid line shows the best-fit resulting from the combined contribution from three different relaxation routes: a QTM, a field-induced direct process, and a two-phonon Raman relaxation process. The contributions from each of these processes are shown by coloured dotted lines. They were obtained using the equation (1) by treating each term (each relaxation process) separately and calculating the related relaxation time (at the specific H and T) using the final fitting parameters obtained from the experimental H - and T -dependences of the overall relaxation time. Each contribution was presented in the form of $\ln(\tau)-T^{-1}$ plot in the temperature range matching the gathered experimental data.

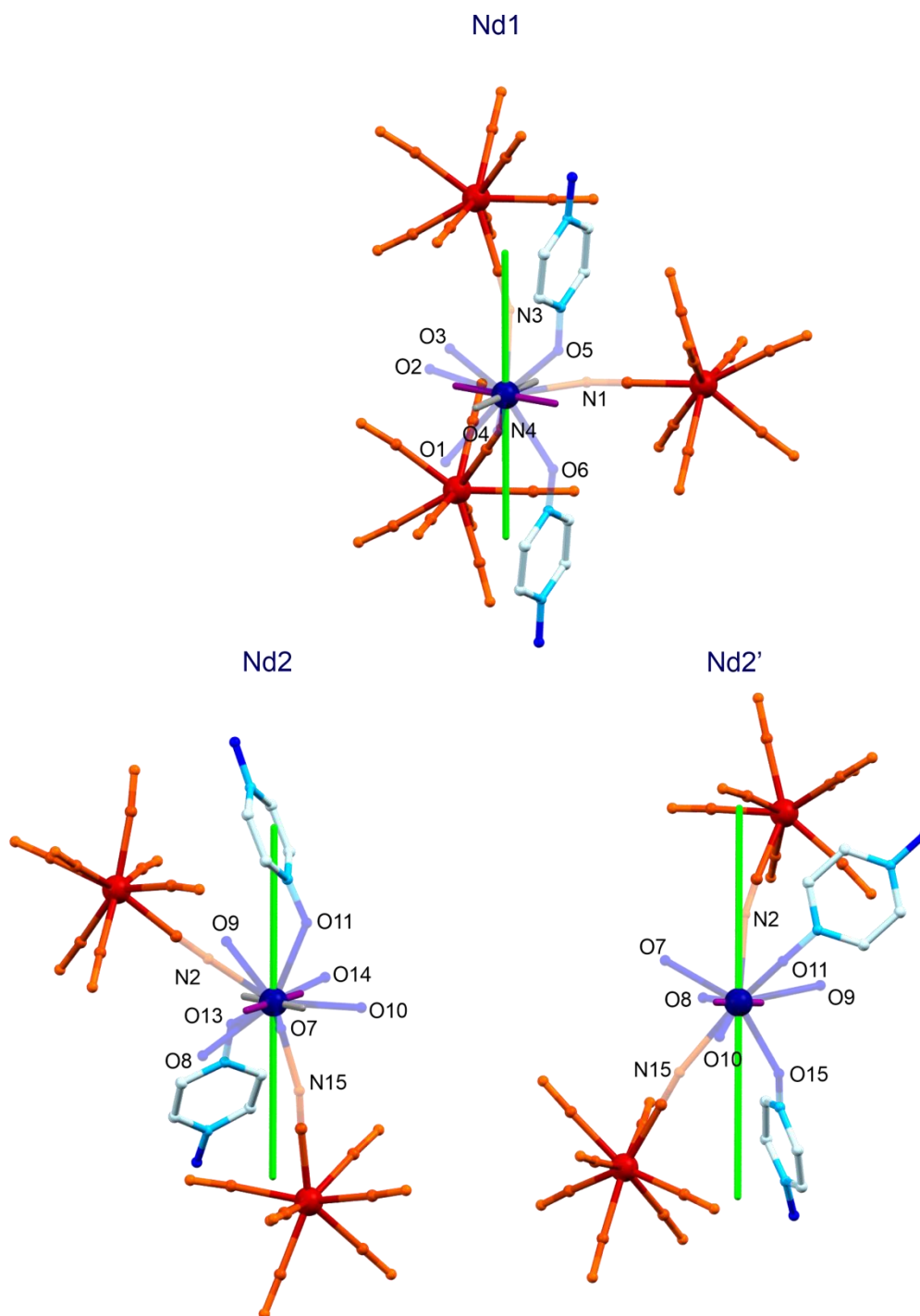


Fig. S18 The representative fragments of the crystal structure of **1a** used for the *ab initio* calculations with the labelling scheme for atoms directly coordinated to each Nd^{III} centre, shown together with the pseudo-*g*-tensor components for the ground Kramers doublets which were calculated using the L basis set (Table S9). The pseudo-*g*-tensor components were visualized by grey (g_x), violet (g_y), and green (g_z) sticks whose relative length illustrates the values of *g*-factor components.

Table S7 Description of the basis sets of two different models: small **S** and large **L**, employed in the *ab initio* calculations of the crystal field effect of Nd^{III} complexes in **1a**.

Basis set S	Basis set L
Nd.ANO-RCC-VDZP 7S6P4D2F1G	Nd.ANO-RCC-VTZP 8S7P5D3F2G1H
Mo.ANO-RCC-VDZ 6S5P3D	Mo.ANO-RCC-VDZ 6S5P3D
N.ANO-RCC-VDZ 3S2P	N.ANO-RCC-VDZ 3S2P (distant atoms) N.ANO-RCC-VDZP 3S2P1D (first coordination sphere)
O.ANO-RCC-VDZ 3S2P	O.ANO-RCC-VDZ 3S2P (distant atoms) O.ANO-RCC-VDZP 3S2P1D (first coordination sphere)
C.ANO-RCC-VDZ 3S2P	C.ANO-RCC-VDZ 3S2P
H.ANO-RCC-VDZ 2S	H.ANO-RCC-VDZ 2S

Table S8 The energy splitting (in cm⁻¹) of the ground ⁴I_{9/2} multiplet of Nd^{III} complexes (Nd1, Nd2, and Nd2' centres) in **1a** obtained using the *ab initio* calculations with the small (S) and large (L) basis sets (Table S7).

Nd1		Nd2		Nd2'	
S	L	S	L	S	L
0	0	0	0	0	0
85.36	92.73	110.94	127.04	126.72	136.31
143.20	171.42	157.77	175.67	252.36	275.94
264.36	286.98	259.95	287.79	293.26	323.97
292.43	314.38	282.85	308.23	396.54	432.09

Table S9 Pseudo-*g*-tensor components for all Kramers doublets of the respective ground multiplets for Nd^{III} complexes (Nd1, Nd2, and Nd2') of **1a** obtained from the *ab initio* calculations using two indicated basis sets (Table S7).

Nd ^{III} centre / no. of sublevel		pseudo- <i>g</i> -factor components					
		<i>g_x</i>		<i>g_y</i>		<i>g_z</i>	
		S basis	L basis	S basis	L basis	S basis	L basis
Nd1	1	1.4521	1.5559	1.5473	1.6555	4.2894	4.1478
	2	0.0996	0.3305	1.7595	1.5389	3.8139	4.099
	3	3.8241	0.4279	2.2058	1.7597	0.2477	3.9251
	4	0.5325	3.2676	1.4309	2.0123	3.6863	0.6247
	5	0.2006	0.1298	1.7574	1.6023	4.4631	4.7315
Nd2	1	1.1134	1.0135	1.2285	1.2071	4.8962	4.9526
	2	0.0481	0.0447	0.734	0.8706	4.6069	4.3282
	3	0.7494	1.0065	1.5766	1.382	3.3474	3.5403
	4	3.3221	0.2636	2.607	1.7127	0.5485	3.8867
	5	0.004	0.3217	1.5658	1.6222	3.1563	3.5361
Nd2'	1	0.1373	0.1845	0.5593	0.6323	5.4502	5.4265
	2	0.2098	0.2436	1.0489	0.822	3.9445	4.1134
	3	0.0255	0.2325	1.2184	1.4729	4.0246	3.9578
	4	0.1281	0.2192	1.7112	1.4557	3.5848	3.8937
	5	0.1089	0.1273	0.691	0.6662	5.9175	5.9475

Table S10 Composition of the ground Kramers doublets in the m_j basis on the quantization axis within the ground $J = 9/2$ manifold, obtained from the *ab initio* calculations using the L basis set. In each case, the first row shows the states with contribution above 5%, the second row lying in the 5–2% range, the third row lying in the 2–1% range, and the last row shows the states with minor contributions below 1%.

Nd ^{III} centre	Composition
Nd1	<p style="text-align: center;">$\pm 7/2$, 73.0%; $\pm 5/2$, 7.1%; $\mp 7/2$, 6.5%; $\mp 5/2$, 5.1%; $\pm 9/2$, 4.4%; $\mp 3/2$, 1.9%; $\pm 3/2$, 0.7%; $\mp 1/2$, 0.6%; $\pm 1/2$, 0.5%; $\mp 9/2$, 0.2%</p>
Nd2	<p style="text-align: center;">$\pm 9/2$, 65.9%; $\pm 1/2$, 15.3%; $\pm 5/2$, 8.7%; $\mp 9/2$, 4.4%; $\pm 3/2$, 2.1%; $\mp 1/2$, 1.9%; $\mp 3/2$, 0.7%; $\mp 7/2$, 0.6%; $\mp 5/2$, 0.4%; $\pm 7/2$, 0.0%</p>
Nd2'	<p style="text-align: center;">$\pm 9/2$, 67.6%; $\pm 5/2$, 10.2%; $\pm 3/2$, 8.1%; $\pm 7/2$, 4.7%; $\mp 9/2$, 4.4%; $\pm 1/2$, 1.7%; $\mp 7/2$, 1.6%; $\mp 5/2$, 1.4%; $\mp 3/2$, 0.2%; $\mp 1/2$, 0.2%</p>

Table S11 The crystal-field parameters, B_k^q , of Nd1 complex in **1a** obtained from the *ab initio* calculations using two different **S** and **L** basis sets (Table S7).

B_k^q		value of B_q^k for Nd1 in the S basis / cm^{-1}	value of B_q^k for Nd1 in the L basis / cm^{-1}	B_k^q		value of B_q^k for Nd1 in the S basis / cm^{-1}	value of B_q^k for Nd1 in the L basis / cm^{-1}
k	q			k	q		
2	-2	-0.38038	0.00543	6	2	$1.55261 \cdot 10^{-4}$	$7.01235 \cdot 10^{-4}$
2	-1	-0.25371	-0.29158	6	3	$-5.12721 \cdot 10^{-4}$	$-6.09184 \cdot 10^{-5}$
2	0	-1.17899	-1.56561	6	4	-0.00117	0.00101
2	1	-0.18476	-0.27512	6	5	$-4.48948 \cdot 10^{-4}$	$-4.40125 \cdot 10^{-4}$
2	2	0.35241	-0.21071	6	6	-0.00115	0.00169
4	-4	0.00329	-0.00387	8	-8	$1.20411 \cdot 10^{-7}$	$1.47879 \cdot 10^{-7}$
4	-3	0.00826	$-7.55902 \cdot 10^{-4}$	8	-7	$-2.97825 \cdot 10^{-6}$	$2.45665 \cdot 10^{-6}$
4	-2	-0.00395	-0.0104	8	-6	$-4.32231 \cdot 10^{-7}$	$4.27554 \cdot 10^{-7}$
4	-1	0.01835	0.00968	8	-5	$1.76381 \cdot 10^{-6}$	$-1.80654 \cdot 10^{-6}$
4	0	0.01513	0.01739	8	-4	$6.78097 \cdot 10^{-7}$	$1.41186 \cdot 10^{-8}$
4	1	$-2.85252 \cdot 10^{-4}$	0.01042	8	-3	$1.21923 \cdot 10^{-6}$	$-1.32421 \cdot 10^{-7}$
4	2	0.00319	0.00712	8	-2	$2.93746 \cdot 10^{-7}$	$-3.44028 \cdot 10^{-8}$
4	3	$-6.60078 \cdot 10^{-4}$	0.0061	8	-1	$4.86531 \cdot 10^{-8}$	$6.01182 \cdot 10^{-7}$
4	4	0.00152	0.00498	8	0	$-8.65567 \cdot 10^{-7}$	$-5.24063 \cdot 10^{-7}$
6	-6	$3.97402 \cdot 10^{-4}$	$1.64566 \cdot 10^{-4}$	8	1	$4.82266 \cdot 10^{-7}$	$1.62517 \cdot 10^{-7}$
6	-5	-0.00155	0.00109	8	2	$-4.60466 \cdot 10^{-7}$	$-1.71827 \cdot 10^{-7}$
6	-4	$-1.83026 \cdot 10^{-5}$	0.00106	8	3	$1.99829 \cdot 10^{-7}$	$1.21866 \cdot 10^{-6}$
6	-3	$-2.95078 \cdot 10^{-5}$	$-1.35956 \cdot 10^{-4}$	8	4	$-1.22305 \cdot 10^{-6}$	$-4.12766 \cdot 10^{-8}$
6	-2	$-8.50297 \cdot 10^{-4}$	$-4.02188 \cdot 10^{-4}$	8	5	$2.4721 \cdot 10^{-8}$	$7.02991 \cdot 10^{-7}$
6	-1	0.0023	0.00169	8	6	$-1.12372 \cdot 10^{-6}$	$1.87401 \cdot 10^{-6}$
6	0	$3.8133 \cdot 10^{-4}$	0.00122	8	7	$3.85715 \cdot 10^{-7}$	$1.21398 \cdot 10^{-6}$
6	1	$-3.99792 \cdot 10^{-4}$	$9.06819 \cdot 10^{-4}$	8	8	$2.17218 \cdot 10^{-7}$	$6.40565 \cdot 10^{-7}$

Table S12 The crystal-field parameters, B_k^q , of Nd2 complex in **1a** obtained from the *ab initio* calculations using two different **S** and **L** basis sets (Table S7).

B_k^q		value of B_q^k for Nd2 in the S basis / cm^{-1}	value of B_q^k for Nd2 in the L basis / cm^{-1}	B_k^q		value of B_q^k for Nd2 in the S basis / cm^{-1}	value of B_q^k for Nd2 in the L basis / cm^{-1}
k	q			k	q		
2	-2	1.13872	1.42997	6	2	$-5.46538 \cdot 10^{-5}$	$-4.22347 \cdot 10^{-4}$
2	-1	-1.04717	-0.93803	6	3	$4.68524 \cdot 10^{-4}$	$3.62139 \cdot 10^{-4}$
2	0	-1.95476	-2.30458	6	4	-0.00201	$-3.00588 \cdot 10^{-4}$
2	1	-0.07793	0.16657	6	5	$-2.62439 \cdot 10^{-4}$	$8.12264 \cdot 10^{-4}$
2	2	1.02505	0.87126	6	6	$4.80617 \cdot 10^{-4}$	$6.35178 \cdot 10^{-4}$
4	-4	-0.01643	-0.00958	8	-8	$2.11901 \cdot 10^{-6}$	$2.84343 \cdot 10^{-7}$
4	-3	0.00116	0.00495	8	-7	$1.54199 \cdot 10^{-7}$	$-2.04353 \cdot 10^{-7}$
4	-2	0.02012	0.02183	8	-6	$8.83099 \cdot 10^{-7}$	$-5.15511 \cdot 10^{-7}$
4	-1	0.00327	0.00103	8	-5	$1.02799 \cdot 10^{-6}$	$3.12046 \cdot 10^{-7}$
4	0	-0.00881	-0.00966	8	-4	$2.04994 \cdot 10^{-7}$	$-3.67776 \cdot 10^{-7}$
4	1	-0.00331	-0.0045	8	-3	$4.9565 \cdot 10^{-7}$	$8.17065 \cdot 10^{-9}$
4	2	0.00525	-0.00393	8	-2	$2.46127 \cdot 10^{-7}$	$2.19467 \cdot 10^{-7}$
4	3	0.00811	0.00528	8	-1	$2.99552 \cdot 10^{-7}$	$3.9969 \cdot 10^{-7}$
4	4	$4.03615 \cdot 10^{-4}$	0.01354	8	0	$1.04342 \cdot 10^{-7}$	$3.9449 \cdot 10^{-8}$
6	-6	$-4.21996 \cdot 10^{-4}$	$4.07371 \cdot 10^{-4}$	8	1	$4.11382 \cdot 10^{-7}$	$3.03945 \cdot 10^{-7}$
6	-5	$-9.64321 \cdot 10^{-4}$	$-6.6818 \cdot 10^{-4}$	8	2	$-1.00734 \cdot 10^{-7}$	$-2.65073 \cdot 10^{-7}$
6	-4	-0.00123	-0.0025	8	3	$-5.6598 \cdot 10^{-7}$	$-8.46451 \cdot 10^{-7}$
6	-3	$1.29543 \cdot 10^{-4}$	$4.1539 \cdot 10^{-4}$	8	4	$-5.35403 \cdot 10^{-7}$	$-4.97351 \cdot 10^{-7}$
6	-2	$7.38003 \cdot 10^{-4}$	$7.44747 \cdot 10^{-4}$	8	5	$-2.31873 \cdot 10^{-7}$	$-1.17612 \cdot 10^{-6}$
6	-1	$6.53317 \cdot 10^{-4}$	$7.19359 \cdot 10^{-4}$	8	6	$-6.29952 \cdot 10^{-7}$	$-1.25541 \cdot 10^{-6}$
6	0	$-2.42469 \cdot 10^{-4}$	$-2.80473 \cdot 10^{-4}$	8	7	$-1.43566 \cdot 10^{-7}$	$-1.60281 \cdot 10^{-7}$
6	1	$2.23764 \cdot 10^{-4}$	$1.11494 \cdot 10^{-4}$	8	8	$6.857 \cdot 10^{-7}$	$-2.55253 \cdot 10^{-6}$

Table S13 The crystal-field parameters, B_k^q , of Nd2' complex in **1a** obtained from the *ab initio* calculations using two different **S** and **L** basis sets (Table S7).

B_k^q		value of B_q^k for Nd2' in the S basis / cm^{-1}	value of B_q^k for Nd2' in the L basis / cm^{-1}	B_k^q		value of B_q^k for Nd2' in the S basis / cm^{-1}	value of B_q^k for Nd2' in the L basis / cm^{-1}
k	q			k	q		
2	-2	2.58987	2.80057	6	2	$6.35016 \cdot 10^{-4}$	$7.42815 \cdot 10^{-4}$
2	-1	-0.92275	-0.94249	6	3	-0.0011	-0.0014
2	0	-3.686	-4.05672	6	4	$-4.06836 \cdot 10^{-4}$	$-4.35369 \cdot 10^{-4}$
2	1	-0.28973	-0.14234	6	5	$-1.07779 \cdot 10^{-4}$	$-5.14631 \cdot 10^{-5}$
2	2	0.69288	1.28124	6	6	$6.96964 \cdot 10^{-4}$	0.00104
4	-4	0.01602	0.02346	8	-8	$3.5358 \cdot 10^{-7}$	$1.65727 \cdot 10^{-7}$
4	-3	-0.03585	-0.03474	8	-7	$-5.04604 \cdot 10^{-7}$	$1.43571 \cdot 10^{-7}$
4	-2	0.00735	0.00203	8	-6	$1.29745 \cdot 10^{-7}$	$6.11913 \cdot 10^{-7}$
4	-1	0.01442	0.01847	8	-5	$-9.59017 \cdot 10^{-7}$	$-1.14755 \cdot 10^{-6}$
4	0	-0.00105	-0.00219	8	-4	$3.35284 \cdot 10^{-7}$	$3.45144 \cdot 10^{-7}$
4	1	-0.00987	-0.00901	8	-3	$4.07591 \cdot 10^{-7}$	$6.77601 \cdot 10^{-7}$
4	2	0.02166	0.02644	8	-2	$6.65493 \cdot 10^{-7}$	$8.03837 \cdot 10^{-7}$
4	3	-0.01046	-0.02207	8	-1	$1.50166 \cdot 10^{-7}$	$2.63161 \cdot 10^{-7}$
4	4	-0.02698	-0.01924	8	0	$-5.77736 \cdot 10^{-7}$	$-7.72585 \cdot 10^{-7}$
6	-6	$6.18091 \cdot 10^{-4}$	$1.34894 \cdot 10^{-4}$	8	1	$6.93106 \cdot 10^{-7}$	$6.54141 \cdot 10^{-7}$
6	-5	$7.94596 \cdot 10^{-5}$	$1.05017 \cdot 10^{-4}$	8	2	$4.46833 \cdot 10^{-7}$	$7.63952 \cdot 10^{-7}$
6	-4	$-1.97051 \cdot 10^{-4}$	$-2.48793 \cdot 10^{-4}$	8	3	$-1.54729 \cdot 10^{-8}$	$7.91038 \cdot 10^{-8}$
6	-3	-0.00119	$-8.67545 \cdot 10^{-4}$	8	4	$7.39562 \cdot 10^{-8}$	$1.72202 \cdot 10^{-7}$
6	-2	$2.68446 \cdot 10^{-4}$	$-1.05663 \cdot 10^{-4}$	8	5	$2.05796 \cdot 10^{-7}$	$-3.72913 \cdot 10^{-7}$
6	-1	$1.80001 \cdot 10^{-4}$	$2.8619 \cdot 10^{-4}$	8	6	$-4.65965 \cdot 10^{-7}$	$-3.99894 \cdot 10^{-7}$
6	0	$-6.70917 \cdot 10^{-4}$	$-7.57821 \cdot 10^{-4}$	8	7	$-8.00426 \cdot 10^{-7}$	$-1.29518 \cdot 10^{-6}$
6	1	-0.00188	-0.00208	8	8	$1.55351 \cdot 10^{-7}$	$5.16365 \cdot 10^{-7}$

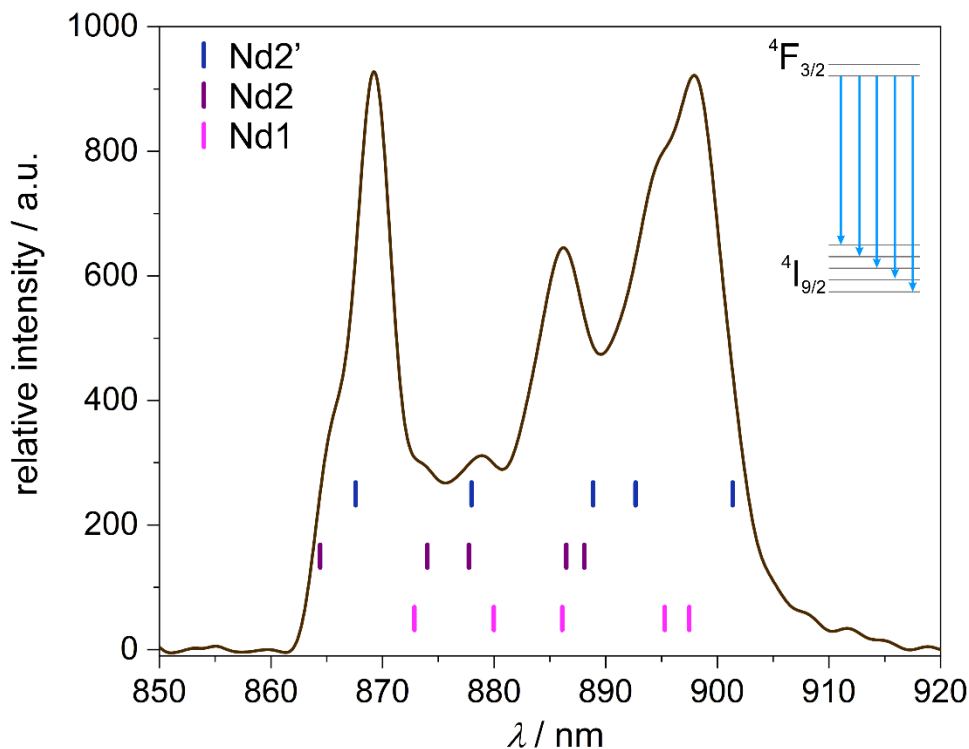


Fig. S19 Low-temperature (77 K) high-resolution emission spectrum of **1** under the 410 nm excitation (solid black line), shown in the limited part related to the ${}^4F_{3/2} \rightarrow {}^4I_{9/2}$ electronic transition, and correlated with the energy splitting schemes of the ground ${}^4I_{9/2}$ multiplets of three incorporated Nd^{III} complexes (Nd1, Nd2, Nd2'; coloured bars) which were obtained from the *ab initio* calculations using the large basis set (Tables S7–S8). The bars lying at the highest energy for each Nd^{III} centre is assignable to the energy difference between the bottoms of the ground and excited multiplets. These starting points were positioned to obtain the best representation of the emission pattern using all other m_j states of the ground multiplets of Nd^{III} complexes. The visualization of the considered electronic transitions is shown in the inset. Only the electronic transitions from the bottom of the excited (emissive) ${}^4F_{3/2}$ multiplet were considered. The overlapping hot bands originating from the electronic transitions from a higher lying m_j state of the emissive multiplet cannot be neglected at 77 K. However, the resulting peaks are expected to be relatively weak at this temperature, giving rather minor contribution to the observed emission pattern.